The Astrophysical Journal, 716:993–1011, 2010 June 20 doi:10.1088/0004-637X/716/2/993
© 2010. The American Astronomical Society. All rights reserved. Printed in the U.S.A.

THE LICK AGN MONITORING PROJECT: REVERBERATION MAPPING OF OPTICAL HYDROGEN AND HELIUM RECOMBINATION LINES

Misty C. Bentz[1,17], Jonelle L. Walsh[1], Aaron J. Barth[1], Yuzuru Yoshii[2], Jong-Hak Woo[3,4], Xiaofeng Wang[5,6,7], Tommaso Treu[8,18], Carol E. Thornton[1], Rachel A. Street[8,9], Thea N. Steele[5], Jeffrey M. Silverman[5], Frank J. D. Serduke[5], Yu Sakata[2,10], Takeo Minezaki[2], Matthew A. Malkan[3], Weidong Li[5], Nicholas Lee[5,11], Kyle D. Hiner[12,13], Marton G. Hidas[8,9,14], Jenny E. Greene[15,19], Elinor L. Gates[16], Mohan Ganeshalingam[5], Alexei V. Filippenko[5], Gabriela Canalizo[12,13], Vardha Nicola Bennert[8,12], and Nairn Baliber[8,9]
[1] Department of Physics and Astronomy, 4129 Frederick Reines Hall, University of California, Irvine, CA 92697, USA; mbentz@uci.edu
[2] Institute of Astronomy, School of Science, University of Tokyo, 2-21-1 Osawa, Mitaka, Tokyo 181-0015, Japan
[3] Department of Physics and Astronomy, University of California, Los Angeles, CA 90024, USA
[4] Astronomy Program, Department of Physics and Astronomy, Seoul National University, Gwanak-gu, Seoul 151-742, Korea
[5] Department of Astronomy, University of California, Berkeley, CA 94720-3411, USA
[6] Physics Department and Tsinghua Center for Astrophysics (THCA), Tsinghua University, Beijing 100084, China
[7] Physics Department, Texas A&M University, College Station, TX 77843-4242, USA
[8] Physics Department, University of California, Santa Barbara, CA 93106, USA
[9] Las Cumbres Observatory Global Telescope, 6740 Cortona Dr. Ste. 102, Goleta, CA 93117, USA
[10] Department of Astronomy, School of Science, University of Tokyo, 7-3-1 Hongo, Bunkyo-ku, Tokyo 113-0033, Japan
[11] Institute for Astronomy, 2680 Woodlawn Dr., Honolulu, HI 96822, USA
[12] Institute of Geophysics and Planetary Physics, University of California, Riverside, CA 92521, USA
[13] Department of Physics and Astronomy, University of California, Riverside, CA 92521, USA
[14] Sydney Institute for Astronomy, School of Physics, The University of Sydney, NSW 2006, Australia
[15] Princeton University Observatory, Princeton, NJ 08544, USA
[16] Lick Observatory, P.O. Box 85, Mount Hamilton, CA 95140, USA
Received 2009 December 18; accepted 2010 April 16; published 2010 May 26

ABSTRACT

We have recently completed a 64-night spectroscopic monitoring campaign at the Lick Observatory 3 m Shane telescope with the aim of measuring the masses of the black holes in 12 nearby ($z < 0.05$) Seyfert 1 galaxies with expected masses in the range $\sim 10^6$–$10^7\ M_\odot$ and also the well-studied nearby active galactic nucleus (AGN) NGC 5548. Nine of the objects in the sample (including NGC 5548) showed optical variability of sufficient strength during the monitoring campaign to allow for a time lag to be measured between the continuum fluctuations and the response to these fluctuations in the broad Hβ emission, which we have previously reported. We present here the light curves for the Hα, Hγ, He II λ4686, and He I λ5876 emission lines and the time lags for the emission-line responses relative to changes in the continuum flux. Combining each emission-line time lag with the measured width of the line in the variable part of the spectrum, we determine a virial mass of the central supermassive black hole from several independent emission lines. We find that the masses are generally consistent within the uncertainties. The time-lag response as a function of velocity across the Balmer line profiles is examined for six of the AGNs. We find similar responses across all three Balmer lines for Arp 151, which shows a strongly asymmetric profile, and for SBS 1116+583A and NGC 6814, which show a symmetric response about zero velocity. For the other three AGNs, the data quality is somewhat lower and the velocity-resolved time-lag response is less clear. Finally, we compare several trends seen in the data set against the predictions from photoionization calculations as presented by Korista & Goad. We confirm several of their predictions, including an increase in responsivity and a decrease in the mean time lag as the excitation and ionization level for the species increases. Specifically, we find the time lags of the optical recombination lines to have weighted mean ratios of τ(Hα):τ(Hβ):τ(Hγ):τ(He I):τ(He II)= 1.54:1.00:0.61:0.36:0.25. Further confirmation of photoionization predictions for broad-line gas behavior will require additional monitoring programs for these AGNs while they are in different luminosity states.

Key words: galaxies: active – galaxies: nuclei – galaxies: Seyfert

Online-only material: color figures, machine-readable tables

1. INTRODUCTION

Active galactic nuclei (AGNs) are some of the most energetic objects in the universe, radiating at luminosities above 10^{42} erg s^{-1}, and yet their continuum emission is known to vary on timescales as short as days. The size constraints set by such rapid variability mean that the extreme energy output of AGNs, often comparable to or more than the energy output of all the stars in a typical galaxy, must originate within a region whose size is $\sim$0.01 pc (approximately the size of our solar system). This large amount of energy arising from such a small region is theorized to be the result of gravitational accretion onto a supermassive black hole (e.g., Rees 1984).

For even the nearest AGNs, the region in which the continuum emission arises is only microarcseconds in angular size and is therefore unresolvable with current imaging detectors. Dedicated monitoring programs have instead taken advantage of the fast, and often dramatic, variability of AGNs to completely

[17] Hubble Fellow.
[18] Sloan Fellow and Packard Fellow.
[19] Carnegie-Princeton Fellow.

revise our understanding of the physical conditions present in the gas on these small scales.

Early monitoring programs with monthly sampling found that variations in the broad emission lines promptly followed variations in the continuum flux, putting an upper limit on the size of the broad-line region (BLR) of only a light-month for typical Seyfert galaxies (e.g., NGC 4151: Antonucci & Cohen 1983; Ark 120: Peterson et al. 1985). Especially, in the case of Ark 120, this upper limit was surprising, as the size of the BLR was expected to be an order of magnitude larger, based on photoionization models (e.g., Kwan & Krolik 1981; Ferland & Mushotzky 1982). Higher temporal sampling has since confirmed the size of the BLR for typical nearby Seyferts to be only a few light-days.

In addition, densely sampled monitoring programs have discovered that higher ionization lines respond more promptly (and more strongly) to continuum variations than lower ionization lines (e.g., Clavel et al. 1991), indicating radial ionization stratification throughout the BLR, contrary to the previous single-cloud models where all emission lines were thought to arise from the same location. More recent models such as the "locally optimally emitting cloud" (LOC) model (Baldwin et al. 1995) predict ionization stratification as a natural outcome. In the LOC model, a range of cloud parameters is present in the BLR, and the emission that we happen to see as observers arises from selection effects working within the BLR such that the majority of the emission from a specific line will come from a location where the parameters are most conducive to the production of that line.

A further discovery of monitoring programs is that the BLR appears to be virialized; the distance to a specific region in the BLR is inversely proportional to the square of the gas velocity in that region. This was first conclusively shown for the most well-studied AGN, NGC 5548 (Peterson & Wandel 1999; see also Krolik et al. 1991), where $\tau \propto v^{-2}$, with τ being the broad emission-line time lag relative to changes in the continuum flux (i.e., the BLR light-crossing time), and v the velocity width of the broad line. Subsequent studies have also shown this to be true for several additional AGNs (e.g., Onken & Peterson 2002; Kollatschny 2003). This behavior is consistent with the fact that the BLR gas is under the gravitational dominance of the central supermassive black hole, and so the response of the BLR gas can be used to learn about the mass of the black hole.

To date, black hole masses have been determined for some 44 AGNs (Peterson et al. 2004, 2005; Bentz et al. 2009). The most recent additions come from the Lick AGN Monitoring Program (LAMP), a dedicated 64-night spectroscopic monitoring campaign using the Lick Observatory 3 m Shane telescope and supplemented by four small-aperture telescopes employed in photometric monitoring. First results from LAMP were presented by Bentz et al. (2008, hereafter Paper I), followed by a full presentation of the photometric light curves (Walsh et al. 2009, hereafter Paper II) and the Hβ light curves and analysis (Bentz et al. 2009, hereafter Paper III), and a re-examination of the $M_{\rm BH}$–$\sigma_\star$ relationship for AGNs (Woo et al. 2010, hereafter Paper IV). In this work, we present the light curves and analysis for the additional broad optical emission lines in the LAMP sample, namely Hα, Hγ, He II λ4686, and He Iλ5876. We compare the results for these optical emission lines with results from previous monitoring campaigns, as well as with recent theoretical predictions of BLR behavior based on photoionization models.

2. OBSERVATIONS

The LAMP sample of AGNs is comprised of 12 nearby ($z < 0.05$) Seyfert 1 galaxies with single-epoch black hole mass estimates in the range $\sim 10^6$–$10^7\ M_\odot$, expected Hβ lag times of 5–20 days, and relatively strong broad-line components to their Hβ emission lines. In addition, we include NGC 5548, the most well-studied AGN with over a decade of densely sampled monitoring data and a well-determined black hole mass from reverberation mapping of $6.54^{+0.26}_{-0.25} \times 10^7\ M_\odot$ (Bentz et al. 2007, and references therein), for a total of 13 targets.

Each of the AGNs was monitored both photometrically (Johnson B and V bands) and spectroscopically. Details of the photometric monitoring and data processing are presented in Paper II. In short, four auxiliary telescopes were employed to monitor subsets of the LAMP sample—the 0.76 m robotic Katzman Automatic Imaging Telescope (KAIT), the 2 m Multicolor Active Galactic Nuclei Monitoring telescope, the Palomar 1.5 m telescope, and the 0.8 m Tenagra II telescope. The photometric monitoring began in early 2008 February and was increased to nightly monitoring on 2008 March 17 (UT, both here and throughout), approximately two weeks before the onset of the spectroscopic monitoring. The images were reduced following standard techniques and differential photometry was employed to determine the brightness of the AGNs relative to stars within the field of view. Absolute calibrations were set by observations of Landolt (1992) standard stars. Finally, a simple galaxy disk model was determined for each AGN host galaxy from images obtained on a night with good seeing and clear skies. The modeled disk flux determined to be within the photometric aperture of the AGN was subtracted from the final AGN light curves. No correction has been attempted for the contribution of bulge light, as the bulge and AGN point-spread function are indistinguishable in the ground-based imaging.

Details of the spectroscopic monitoring and processing are presented in Paper III. To summarize, spectroscopic monitoring was carried out over 64 nights at the Lick Observatory 3 m Shane telescope between 2008 March 25 and June 1. The red CCD of the Kast dual spectrograph was employed with the 600 lines mm^{-1} grating (resulting in spectral coverage over 4300–7100 Å), giving a nominal resolution of 2.35 Å pixel^{-1} in the dispersion direction and 0.″78 pixel^{-1} in the spatial direction. A 4″ wide slit was used and each target was observed at a fixed position angle. IRAF[20] was employed for the reduction of the two-dimensional spectroscopic images and the extractions of the one-dimensional spectra. Flux calibrations were determined from nightly spectra of standard stars, which typically included Feige 34 and BD+28°4211. A final, internal calibration of the spectra was accomplished using the spectral scaling algorithm of van Groningen & Wanders (1992). The algorithm scales the total flux of the narrow [O III] $\lambda\lambda$4959, 5007 doublet in each spectrum to match the [O III] flux in a reference spectrum created from the mean of all the spectra for a given object.

As the [O III] doublet is very close in wavelength to the Hβ emission line, the Hβ line is the most accurately calibrated broad line for each of our galaxies. Hα, while being much brighter than Hβ, is $\sim$1700 Å redward of Hβ in the observed frames of these galaxies and is near the red edge of our spectroscopic coverage. Unfortunately, there exists no similar strong, unblended narrow emission line near Hα. The [S II] doublet at $\lambda\lambda$6716, 6731 is

[20] IRAF is distributed by the National Optical Astronomy Observatory, which is operated by the Association of Universities for Research in Astronomy, Inc., under cooperative agreement with the National Science Foundation.

Table 1
Object List

Object	α_{2000} (h m s)	δ_{2000} (° ′ ″)	z	A_B[a] (mag)	Alternate Name
Mrk 142	10 25 31.3	+51 40 35	0.04494	0.069	PG 1022+519
SBS 1116+583A	11 18 57.7	+58 03 24	0.02787	0.050	
Arp 151	11 25 36.2	+54 22 57	0.02109	0.059	Mrk 40
Mrk 1310	12 01 14.3	−03 40 41	0.01941	0.133	
Mrk 202	12 17 55.0	+58 39 35	0.02102	0.087	
NGC 4253	12 18 26.5	+29 48 46	0.01293	0.084	Mrk 766
NGC 4748	12 52 12.4	−13 24 53	0.01463	0.223	
NGC 5548	14 17 59.5	+25 08 12	0.01718	0.088	
NGC 6814	19 42 40.6	−10 19 25	0.00521	0.790	

Note. [a] The Galactic extinction is based on Schlegel et al. (1998).

fairly weak and, at the typical redshifts for the LAMP AGNs ($z \approx 0.01$), was often affected by the atmospheric *B*-band absorption at ∼6860–6890 Å, making it an unacceptable choice for internal scaling of the spectra. Therefore, we have simply applied the scaling determined for the Hβ + [O III] complex to the Hα region as well, even though it may not be entirely accurate due to aperture effects that can vary with wavelength (e.g., differential atmospheric refraction, wavelength-dependent seeing). The Hγ line is much less affected by these issues, as it is closer in wavelength to the Hβ line, although the data quality of Hγ also occasionally suffers from being close to the blue edge of our spectroscopic coverage.

For each of the final, calibrated spectra, spectroscopic light curves were measured by fitting a local, linear continuum under the broad emission line and integrating the emission-line flux above the fitted continuum. This technique includes the flux contribution from the narrow emission lines, but the contribution is just a constant flux offset. Table 1 lists the nine LAMP targets for which we were able to measure Hβ time lags, and Table 2 gives the continuum windows and line integration limits for the

Table 2
Emission-line Continuum Windows and Integration Limits

Object	Line	Continuum (Å)	Windows (Å)	Line Limits (Å)	$\langle f \rangle \pm \sigma_f$ (10^{-13} erg s^{-1} cm^{-2})
Mrk 142	Hα	6700 − 6750	6950 − 7000	6750 − 6950	2.62 ± 0.20
	Hβ	4960 − 5000	5300 − 5350	5045 − 5125	0.928 ± 0.080
	Hγ	4400 − 4450	4580 − 4630	4480 − 4580	0.436 ± 0.043
	He II λ4686	4580 − 4630	4960 − 5000	4750 − 4960	0.70 ± 0.12
	He I λ5876	5825 − 5875	6250 − 6300	6100 − 6200	0.134 ± 0.016
SBS 1116+583A	Hα	6600 − 6650	6950 − 7000	6650 − 6850	1.035 ± 0.071
	Hβ	4875 − 4925	5200 − 5250	4925 − 5055	0.262 ± 0.028
	Hγ	4390 − 4425	4530 − 4580	4425 − 4508	0.129 ± 0.017
	He II λ4686	4650 − 4700	4875 − 4925	4700 − 4875	0.080 ± 0.036
	He I λ5876	5700 − 5800	6200 − 6300	5945 − 6100	0.050 ± 0.017
Arp 151	Hα	6525 − 6575	6900 − 6950	6575 − 6825	3.42 ± 0.42
	Hβ	4850 − 4890	5175 − 5250	4900 − 5040	0.86 ± 0.15
	Hγ	4335 − 4350	4510 − 4530	4390 − 4510	0.365 ± 0.076
	He II λ4686	4620 − 4650	4870 − 4890	4695 − 4870	0.084 ± 0.057
	He I λ5876	5800 − 5875	6225 − 6350	5920 − 6120	0.130 ± 0.041
Mrk 1310	Hα	6525 − 6575	6775 − 6825	6600 − 6775	2.54 ± 0.18
	Hβ	4850 − 4900	5150 − 5200	4900 − 5010	0.495 ± 0.054
	Hγ	4375 − 4395	4525 − 4575	4395 − 4470	0.320 ± 0.026
	He II λ4686	4700 − 4740	4860 − 4900	4740 − 4860	0.035 ± 0.030
	He I λ5876	5750 − 5800	6100 − 6150	5930 − 6040	0.085 ± 0.024
Mrk 202	Hα	6580 − 6630	6800 − 6850	6630 − 6800	1.38 ± 0.11
	Hβ	4875 − 4925	5150 − 5200	4925 − 5025	0.299 ± 0.027
	Hγ	4375 − 4410	4500 − 4550	4410 − 4500	0.159 ± 0.018
	He II λ4686	4500 − 4550	4840 − 4880	4700 − 4840	0.169 ± 0.037
NGC 4253	Hα	6500 − 6550	6850 − 6900	6575 − 6750	11.21 ± 0.47
	Hβ	4820 − 4860	5150 − 5200	4860 − 4975	1.99 ± 0.10
	Hγ	4320 − 4350	4450 − 4500	4350 − 4450	0.646 ± 0.056
NGC 4748	Hα	6500 − 6550	6900 − 6950	6550 − 6750	9.51 ± 0.67
	Hβ	4600 − 4650	5150 − 5200	4850 − 5000	2.11 ± 0.11
	Hγ	4320 − 4360	4450 − 4500	4360 − 4450	1.057 ± 0.066
	He II λ4686	4470 − 4500	5150 − 5200	4660 − 4810	1.17 ± 0.12
NGC 5548	Hα	6300 − 6350	6960 − 7010	6450 − 6900	17.6 ± 1.1
	Hβ	4725 − 4775	5150 − 5200	4775 − 5150	3.39 ± 0.33
	Hγ	4315 − 4340	4500 − 4550	4375 − 4500	0.73 ± 0.14
NGC 6814	Hα	6350 − 6400	6850 − 6900	6450 − 6740	12.62 ± 0.81
	Hβ	4540 − 4590	5100 − 5150	4800 − 4970	2.81 ± 0.26
	Hγ	4317 − 4330	4420 − 4490	4330 − 4415	0.99 ± 0.11
	He II λ4686	4540 − 4590	5100 − 5150	4590 − 4800	0.49 ± 0.24
	He I λ5876	5700 − 5800	5970 − 6020	5820 − 5970	0.49 ± 0.11

Notes. The emission-line fluxes above include the contribution from the narrow-line component, which is simply a constant flux offset. In addition, the Hα fluxes include the contributions from [N II] λλ6548, 6583, and the Hγ fluxes include the contribution from [O III] λ4363.

Table 3
Emission-line Light Curves of Mrk 142

HJD	f(Hα)	f(Hγ)	f(He II)	f(He I)
4550.6599	2.586 ± 0.051	0.436 ± 0.015	0.731 ± 0.030	0.137 ± 0.007
4551.6560	2.448 ± 0.049	0.404 ± 0.014	0.672 ± 0.028	0.116 ± 0.006
4553.6576	2.634 ± 0.052	0.448 ± 0.016	0.680 ± 0.028	0.134 ± 0.007
4555.8322	3.420 ± 0.068	0.566 ± 0.020	1.152 ± 0.048	0.149 ± 0.008
4556.6591	2.581 ± 0.051	0.438 ± 0.015	0.692 ± 0.029	0.126 ± 0.007

Notes. HJD: Heliocentric Julian Day, 2,450,000. Emission-line fluxes are in units of 10^{-13} erg s^{-1} cm^{-2}. The Hβ light curve is presented in Paper III.

(This table is available in its entirety in a machine-readable form in the online journal. A portion is shown here for guidance regarding its form and content.)

Table 4
Emission-line Light Curves of SBS 1116+583A

HJD	f(Hα)	f(Hγ)	f(He II)	f(He I)
4550.6925	11.04 ± 0.34	1.759 ± 0.072	1.215 ± 0.119	0.507 ± 0.099
4551.7189	11.01 ± 0.34	1.552 ± 0.064	0.834 ± 0.082	0.499 ± 0.097
4553.7176	10.53 ± 0.33	1.451 ± 0.060	0.661 ± 0.065	0.559 ± 0.109
4555.8587	11.43 ± 0.35	1.151 ± 0.047	0.830 ± 0.081	...
4556.6866	10.36 ± 0.32	1.328 ± 0.055	0.431 ± 0.042	0.469 ± 0.091

Notes. HJD: Heliocentric Julian Day, 2,450,000. Emission-line fluxes are in units of 10^{-14} erg s^{-1} cm^{-2}. The Hβ light curve is presented in Paper III.

(This table is available in its entirety in a machine-readable form in the online journal. A portion is shown here for guidance regarding its form and content.)

Table 5
Emission-line Light Curves of Arp 151

HJD	f(Hα)	f(Hγ)	f(He II)	f(He I)
4550.7180	3.310 ± 0.061	0.318 ± 0.012	0.017 ± 0.004	0.090 ± 0.010
4551.7478	3.212 ± 0.059	0.318 ± 0.012	0.023 ± 0.005	0.082 ± 0.009
4553.7470	3.031 ± 0.056	0.311 ± 0.012	0.018 ± 0.004	0.085 ± 0.009
4556.7118	3.060 ± 0.057	0.247 ± 0.009	0.040 ± 0.009	0.075 ± 0.008
4557.7555	2.948 ± 0.055	0.245 ± 0.009	0.020 ± 0.005	0.063 ± 0.007

Notes. HJD: Heliocentric Julian Day, 2,450,000. Emission-line fluxes are in units of 10^{-13} erg s^{-1} cm^{-2}. The Hβ light curve is presented in Paper III.

(This table is available in its entirety in a machine-readable form in the online journal. A portion is shown here for guidance regarding its form and content.)

Table 6
Emission-line Light Curves of Mrk 1310

HJD	f(Hα)	f(Hγ)	f(He II)	f(He I)
4550.7726	2.491 ± 0.061	0.288 ± 0.009	0.0321 ± 0.0074	0.076 ± 0.009
4551.8100	2.399 ± 0.059	0.321 ± 0.010	0.0588 ± 0.0135	0.087 ± 0.010
4553.8092	2.476 ± 0.060	0.339 ± 0.010	0.0588 ± 0.0135	0.106 ± 0.012
4556.7724	2.464 ± 0.060	0.354 ± 0.010	0.0583 ± 0.0134	0.127 ± 0.014
4557.8255	2.570 ± 0.063	0.347 ± 0.010	0.0298 ± 0.0068	0.085 ± 0.010

Notes. HJD: Heliocentric Julian Day, 2,450,000. Emission-line fluxes are in units of 10^{-13} erg s^{-1} cm^{-2}. The Hβ light curve is presented in Paper III.

(This table is available in its entirety in a machine-readable form in the online journal. A portion is shown here for guidance regarding its form and content.)

broad, optical emission lines in each of these nine AGNs. Also listed in Table 2 are the means and standard deviations of the emission-line fluxes. In Paper III, we discuss four objects in the LAMP sample which did not have reliable Hβ time lags (IC 4218, MCG-06-30-15, Mrk 290, and IC 1198). We do not find any evidence for reliable time lags in any of the additional optical broad-line light curves from any of these four objects, and so we exclude them from further discussion. Emission-line light curves for the nine LAMP AGNs are presented in Tables 3–11 (we include here the first five epochs of the light curves as a guide; the complete tables are available in the online journal). Figures 1–9 display the *B*- and *V*-band light curves, the emission-line light curves, and the mean and rms spectra for each object.

Table 7
Emission-line Light Curves of Mrk 202

HJD	f(Hα)	f(Hγ)	f(He II)	f(He I)
4550.7434	1.292 ± 0.023	0.1489 ± 0.0048	0.1605 ± 0.0088	0.0489 ± 0.0102
4551.7693	1.247 ± 0.022	0.1574 ± 0.0051	0.1420 ± 0.0078	0.0421 ± 0.0088
4553.7721	1.339 ± 0.024	0.1629 ± 0.0052	0.1707 ± 0.0093	0.0518 ± 0.0108
4556.7381	1.242 ± 0.022	0.1439 ± 0.0046	0.1056 ± 0.0058	0.0476 ± 0.0099
4557.7884	1.259 ± 0.022	0.1460 ± 0.0047	0.1066 ± 0.0058	0.0200 ± 0.0042

Notes. HJD: Heliocentric Julian Day, 2,450,000. Emission-line fluxes are in units of 10^{-13} erg s^{-1} cm^{-2}. The Hβ light curve is presented in Paper III.

(This table is available in its entirety in a machine-readable form in the online journal. A portion is shown here for guidance regarding its form and content.)

Table 8
Emission-line Light Curves of NGC 4253

HJD	f(Hα)	f(Hγ)	f(He II)	f(He I)
4550.8014	10.57 ± 0.25	0.623 ± 0.017	0.628 ± 0.028	0.282 ± 0.011
4551.8338	10.63 ± 0.25	0.653 ± 0.018	0.642 ± 0.029	0.299 ± 0.012
4553.8298	10.61 ± 0.25	0.697 ± 0.019	0.729 ± 0.033	0.295 ± 0.011
4555.9872	10.73 ± 0.25	0.448 ± 0.074	0.590 ± 0.027	0.298 ± 0.052
4556.7926	10.60 ± 0.25	0.690 ± 0.019	0.694 ± 0.031	0.304 ± 0.012

Notes. HJD: Heliocentric Julian Day, 2,450,000. Emission-line fluxes are in units of 10^{-13} erg s^{-1} cm^{-2}. The Hβ light curve is presented in Paper III.

(This table is available in its entirety in a machine-readable form in the online journal. A portion is shown here for guidance regarding its form and content.)

Table 9
Emission-line Light Curves of NGC 4748

HJD	f(Hα)	f(Hγ)	f(He II)	f(He I)
4550.8173	8.65 ± 0.19	0.965 ± 0.023	1.029 ± 0.036	0.329 ± 0.031
4551.8530	8.58 ± 0.19	1.037 ± 0.025	1.004 ± 0.035	0.293 ± 0.027
4553.8454	8.59 ± 0.19	1.040 ± 0.025	1.006 ± 0.035	0.294 ± 0.028
4556.8087	8.31 ± 0.18	0.979 ± 0.023	1.007 ± 0.035	0.342 ± 0.032
4557.8618	8.50 ± 0.19	0.977 ± 0.023	0.888 ± 0.031	0.295 ± 0.028

Notes. HJD: Heliocentric Julian Day, 2,450,000. Emission-line fluxes are in units of 10^{-13} erg s^{-1} cm^{-2}. The Hβ light curve is presented in Paper III.

(This table is available in its entirety in a machine-readable form in the online journal. A portion is shown here for guidance regarding its form and content.)

Table 10
Emission-line Light Curves of NGC 5548

HJD	f(Hα)	f(Hγ)	f(He II)	f(He I)
4550.8678	17.04 ± 0.24	0.802 ± 0.034	0.326 ± 0.054	1.56 ± 0.11
4551.8664	16.97 ± 0.24	0.777 ± 0.033	0.277 ± 0.046	1.73 ± 0.12
4553.8626	16.81 ± 0.23	0.796 ± 0.034	0.283 ± 0.047	1.61 ± 0.11
4556.8589	16.98 ± 0.24	0.753 ± 0.032	0.352 ± 0.058	1.56 ± 0.10
4557.8755	16.80 ± 0.23	0.795 ± 0.034	0.270 ± 0.045	1.56 ± 0.11

Notes. HJD: Heliocentric Julian Day, 2,450,000. Emission-line fluxes are in units of 10^{-13} erg s^{-1} cm^{-2}. The Hβ light curve is presented in Paper III.

(This table is available in its entirety in a machine-readable form in the online journal. A portion is shown here for guidance regarding its form and content.)

Statistical properties of the light curves are listed in Table 12 along with the properties of the *B*- and *V*-band light curves and the 5100 Å flux for comparison. Column 1 lists the object, Column 2 gives the feature, and Column 3 lists the number of measurements in each light curve. Throughout this analysis, we binned all photometric measurements within 0.1 days. Columns 4 and 5 are the sampling intervals between data points, measured as the mean and median, respectively. Column 6 gives the mean fractional error, which is based on the comparison of observations that are closely spaced in time. The "excess variance" in Column 7 is computed as

$$F_{\rm var} = \frac{\sqrt{\sigma^2 - \delta^2}}{\langle f \rangle}, \quad (1)$$

Table 11
Emission-line Light Curves of NGC 6814

HJD	f(Hα)	f(Hγ)	f(He II)	f(He I)
4551.0180	11.79 ± 0.15	0.937 ± 0.026	0.593 ± 0.126	0.381 ± 0.027
4552.0264	11.13 ± 0.14	0.900 ± 0.025	0.163 ± 0.035	0.527 ± 0.038
4556.0339	11.60 ± 0.15	0.934 ± 0.033	0.457 ± 0.097	0.501 ± 0.036
4557.0200	12.15 ± 0.15	1.042 ± 0.029	0.640 ± 0.136	0.566 ± 0.041
4560.0402	12.66 ± 0.16	1.094 ± 0.038	0.902 ± 0.192	0.892 ± 0.064

Notes. HJD: Heliocentric Julian Day, 2,450,000. Emission-line fluxes are in units of 10^{-13} erg s^{-1} cm^{-2}. The Hβ light curve is presented in Paper III.

(This table is available in its entirety in a machine-readable form in the online journal. A portion is shown here for guidance regarding its form and content.)

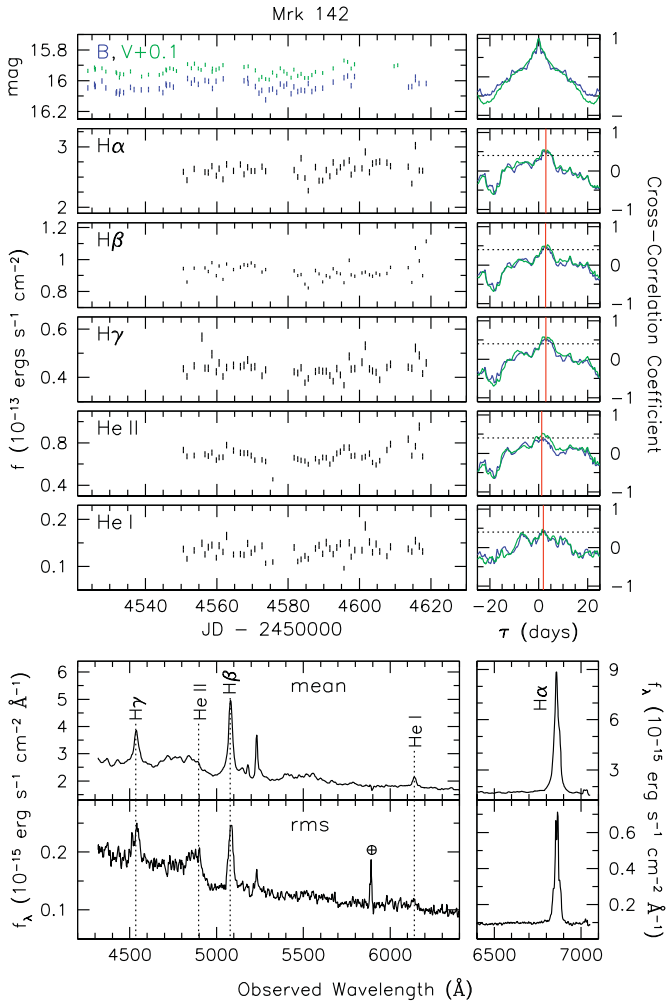

Figure 1. Top: photometric (B- and V-band) and spectroscopic light curves for the permitted broad optical emission lines in Mrk 142. The right panels show the CCFs vs. the B band (blue) and the V band (green). For the photometric light curves, these are the auto-correlation functions. The horizontal dotted line in each CCF panel marks a significance of 0.4, and red vertical lines mark the locations of measured time lags, as listed in Table 13. Bottom: mean and variable (rms) spectra of Mrk 142. The region around Hα has been plotted separately on a different flux scale to allow for ease of viewing the weaker emission features at bluer wavelengths. The spike at 5890 Å is residual noise from the Na I D night-sky line.

(A color version of this figure is available in the online journal.)

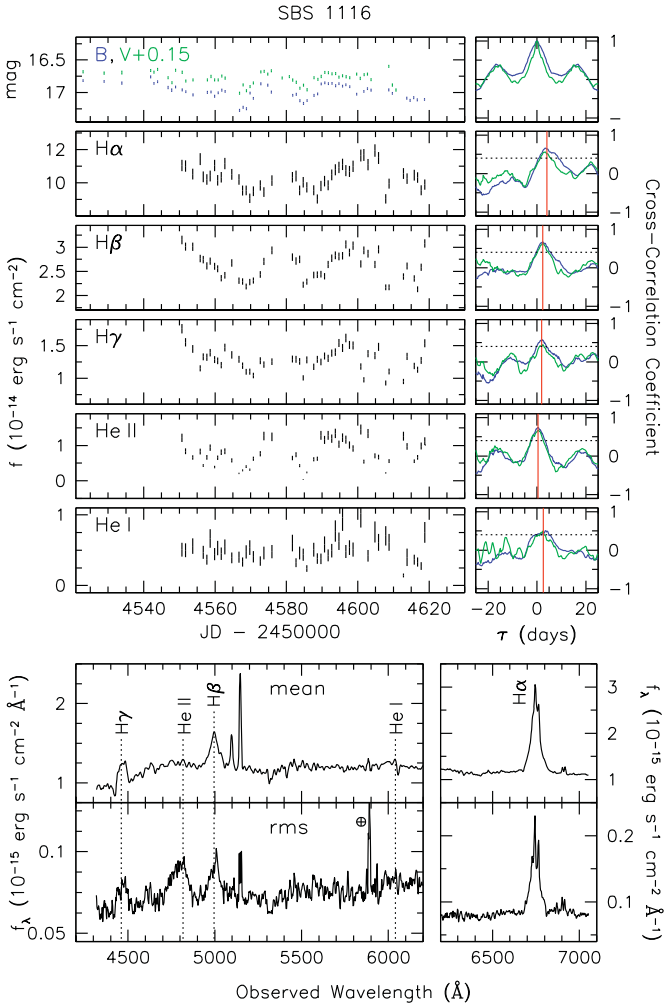

Figure 2. Same as Figure 1, but for SBS 1116.

(A color version of this figure is available in the online journal.)

where σ^2 is the variance of the fluxes, δ^2 is their mean-square uncertainty, and $\langle f \rangle$ is the mean of the observed fluxes. Finally, Column 8 is the ratio of the maximum to the minimum flux ($R_{\rm max}$) for each light curve.

3. ANALYSIS

3.1. Time-series Analysis

For each object, we determined the time lags for all of the broad optical emission lines in the LAMP spectra (Hα, Hβ, Hγ, He II λ4686, and He I λ5876) relative to the two continuum light curves (B and V) measured from the photometric monitoring. In Paper III, we describe in detail the cross-correlation methods

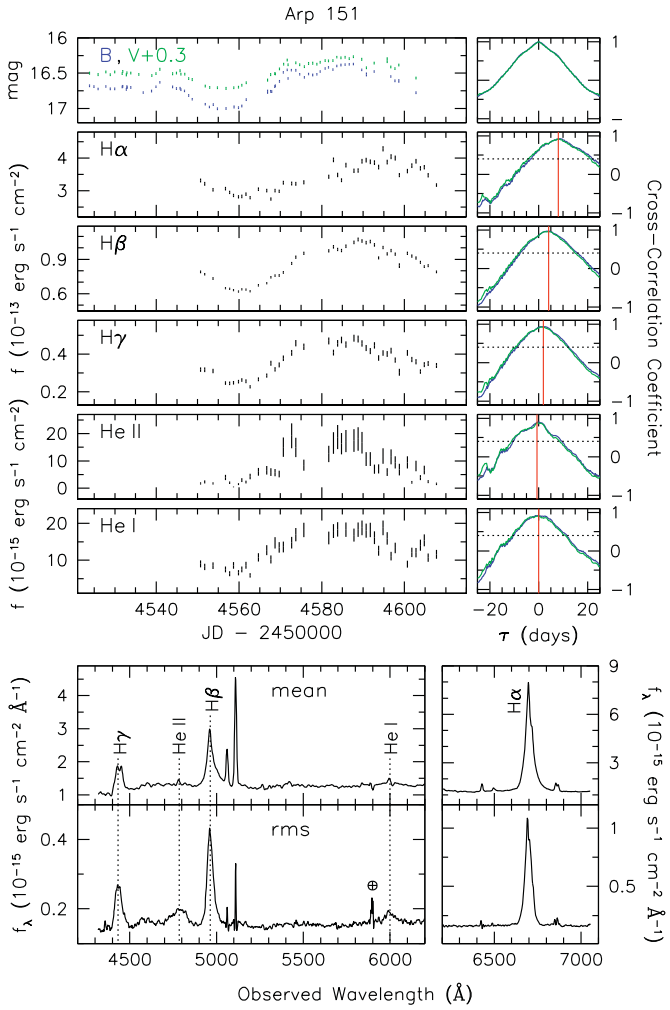

Figure 3. Same as Figure 1, but for Arp 151.
(A color version of this figure is available in the online journal.)

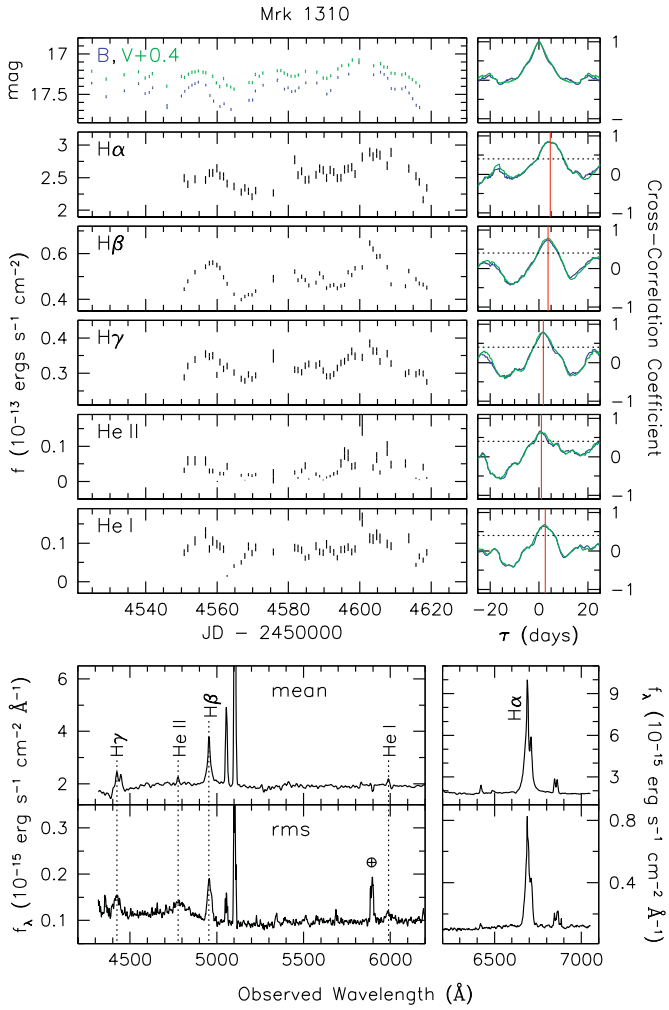

Figure 4. Same as Figure 1, but for Mrk 1310.
(A color version of this figure is available in the online journal.)

used for determining the time lags between the continuum light curves and the broad emission-line light curves. Here we give a brief summary for completeness.

Time lags were measured using the interpolation cross-correlation function (CCF) method of Gaskell & Sparke (1986) and Gaskell & Peterson (1987) with the modifications described by White & Peterson (1994). Cross-correlation functions are characterized by the maximum cross-correlation coefficient ($r_{\rm max}$), the time delay corresponding to the location of $r_{\rm max}$ ($\tau_{\rm peak}$), and the centroid of the points about the peak ($\tau_{\rm cent}$) above some threshold value, typically $0.8r_{\rm max}$. The uncertainties in the time lags were determined using the Monte Carlo "flux randomization/random subset sampling" method described by Peterson et al. (1998, 2004), in which the data points in each light curve are randomly sampled and then randomly altered by a Gaussian deviation of the flux uncertainty. The CCF is calculated for the sampled and modified light curves, and $r_{\rm max}$, $\tau_{\rm cent}$, and $\tau_{\rm peak}$ are measured and recorded. A distribution of measurements is built up from 1000 realizations, and the means of the cross-correlation centroid distribution and the cross-correlation peak distribution are taken to be $\tau_{\rm cent}$ and $\tau_{\rm peak}$, respectively. The uncertainties on $\tau_{\rm cent}$ and $\tau_{\rm peak}$ are defined such that 15.87% of the realizations fall above and 15.87% fall below the range of uncertainties, which, for a Gaussian distribution, would correspond to $\pm 1\sigma$.

Together with the photometric light curves and the broad emission-line light curves in the top panels of Figures 1–9, we also show the cross-correlation (auto-correlation) functions for the emission-line (photometric) light curves. In general, we find reliable time-lag measurements for all three of the Balmer lines in the LAMP spectral coverage. In this case, we define "reliable" as those CCFs for which (1) there is an obvious peak with $\tau \geqslant 0$, (2) the correlations agree for both the *B* and *V* bands, and (3) $r_{\rm max} > 0.4$. The CCFs for the He lines tend to be much noisier than for the Balmer lines and more often fail our definition of reliability. For the reliable lag measurements, Table 13 lists measurements of $\tau_{\rm cent}$ and $\tau_{\rm peak}$ in the observed and rest frame of each AGN for all the emission lines compared to both the *B*- and *V*-band light curves (except for Mrk 202, where we list the "unreliable" measurements for Hα for comparison with the rest of the sample). In the following discussion, we will give preference to lag measurements determined relative to the *B*-band light curve, since the variations in the *B* band are typically stronger than in the *V* band (see Papers II and III for a discussion of this topic).

3.2. Line-width Measurement

The mean and rms spectra for each of the nine AGNs examined here are displayed in the bottom panels of Figures 1–9. The rms spectra show the standard deviation per spectroscopic

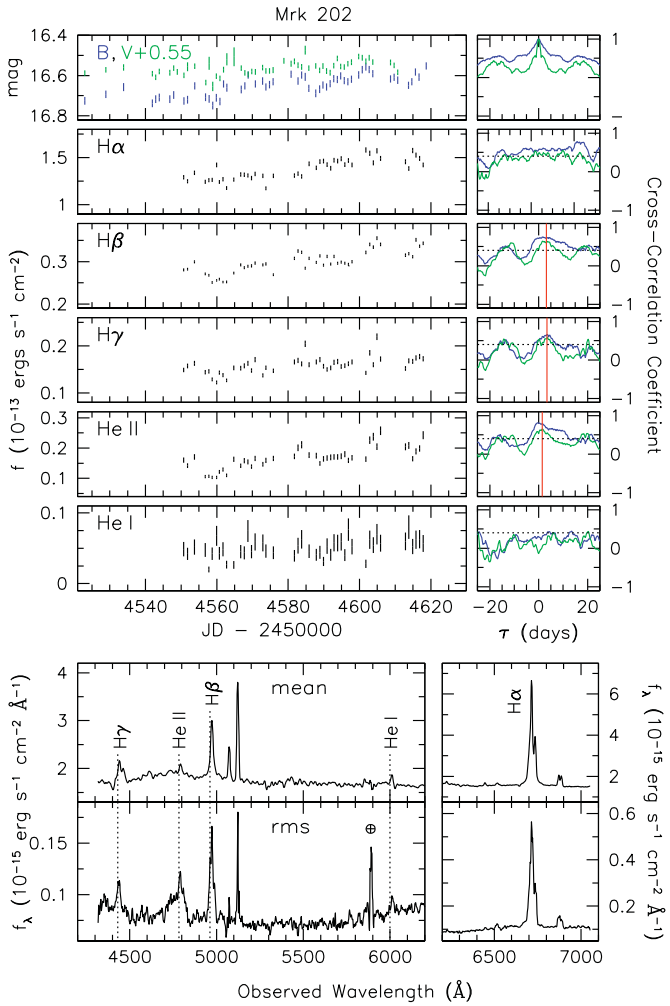

Figure 5. Same as Figure 1, but for Mrk 202.
(A color version of this figure is available in the online journal.)

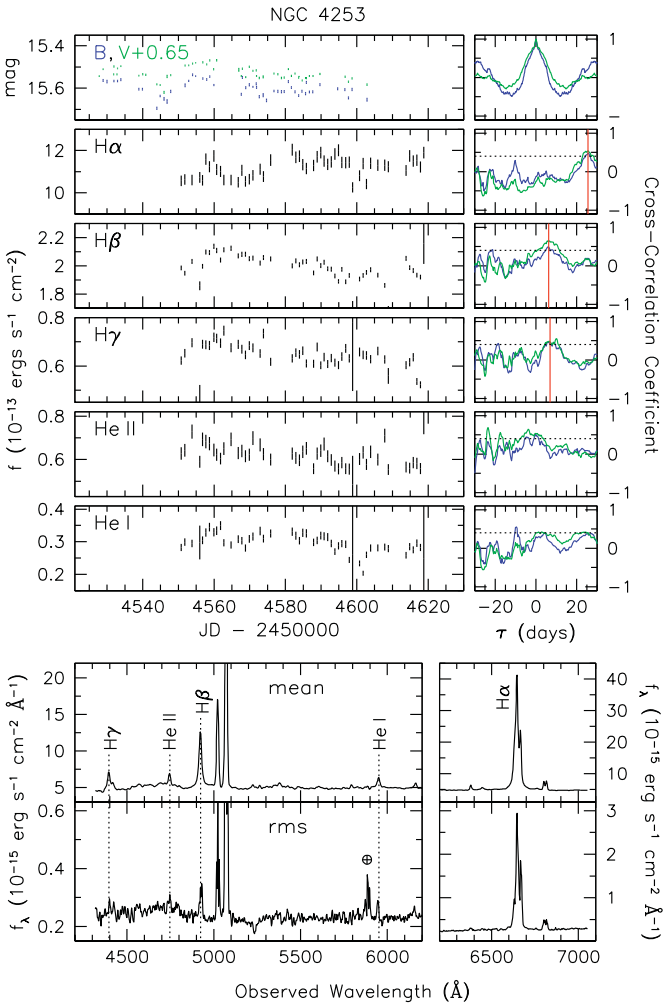

Figure 6. Same as Figure 1, but for NGC 4253.
(A color version of this figure is available in the online journal.)

pixel of all the individual spectra relative to the mean spectrum for an object. Thus, the rms spectra display the variable spectral components.

For each emission line with a measured and reliable time lag, the width of the line was measured in the mean and the rms spectra. The helium lines appear as extremely low-level features in the mean spectra, so only the rms line widths are tabulated when measurements were possible. The details of the techniques for measuring the line widths and their uncertainties are described in Paper III. For each line, we record the width as determined by the full width at half-maximum (FWHM) flux and the second moment of the line profile, the line dispersion ($\sigma_{\rm line}$). Each of the line-width measurements has been corrected for the dispersion of the spectrograph in the manner described in Paper III.

In general, any constant spectral components, such as emission from the host galaxy or narrow-line region (NLR), should disappear in the rms spectra. However, in practice, small errors in spectral calibration and residual aperture effects caused by the combination of a nonzero slit size, atmospheric seeing, and a spatially resolved NLR, are often revealed by emission from constant components that appears in the rms spectra. Unfortunately, several of the objects in the LAMP sample with strong narrow-line emission suffer from this problem in the region of the Hα line. The typical correction for this problem is to remove the narrow-line emission from each individual spectrum in a consistent manner, where the total flux of each narrow line is a constant throughout the spectroscopic campaign, before creating the mean and rms spectra. This method works well for the narrow component of the Hβ line and the narrow [O III] lines in the LAMP spectra, where the spectral calibration is most accurate; however, it does not correct the problem of residual narrow-line emission in the rms profile of Hα. Attempts to remove the narrow Hα and [N II] $\lambda\lambda$6548, 6583 lines in a consistent manner from each individual spectrum cause the residuals to be worsened in the rms spectra. This indicates that the spectral calibration is not completely accurate at the wavelengths around Hα.

Rather than attempting to remove the narrow lines in a manner that is not consistent from spectrum to spectrum (which would introduce further biases into the line-width measurements for Hα), we have revised the uncertainties in the Hα rms line-width measurements to compensate for any bias from residual narrow emission. For each of the objects, the rms Hα profile was interpolated across in an attempt to exclude the narrow emission, and the line width was measured and compared to the width from the uncorrected rms spectrum. For many of the objects, the interpolated line widths fell within the uncertainties for the line-width measurement. For SBS 1116 and NGC 5548, where this was not the case, the rms Hα line-width uncertainty

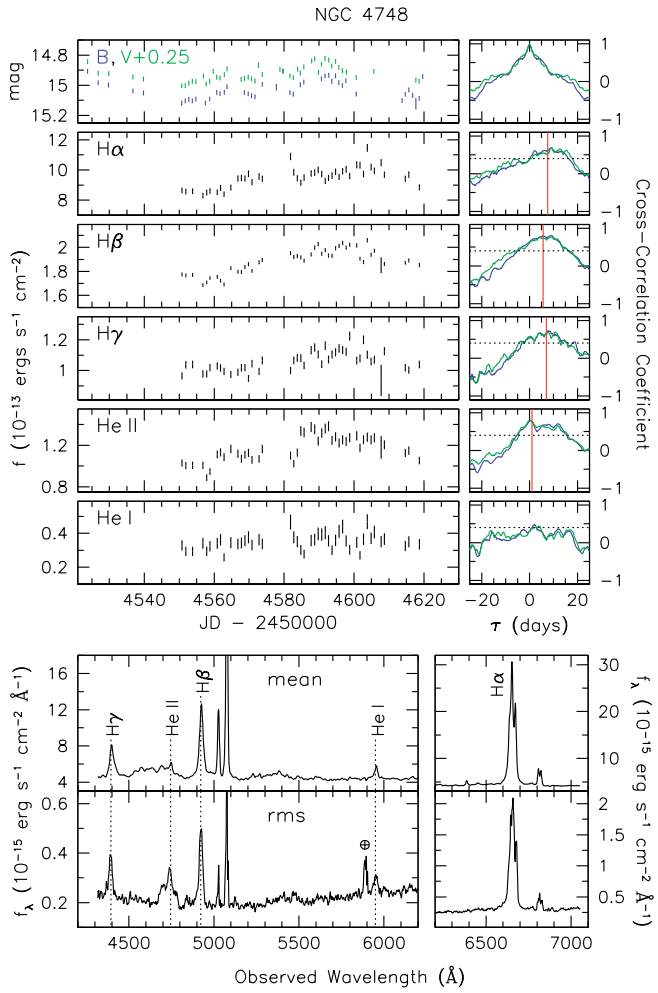

Figure 7. Same as Figure 1, but for NGC 4748.

(A color version of this figure is available in the online journal.)

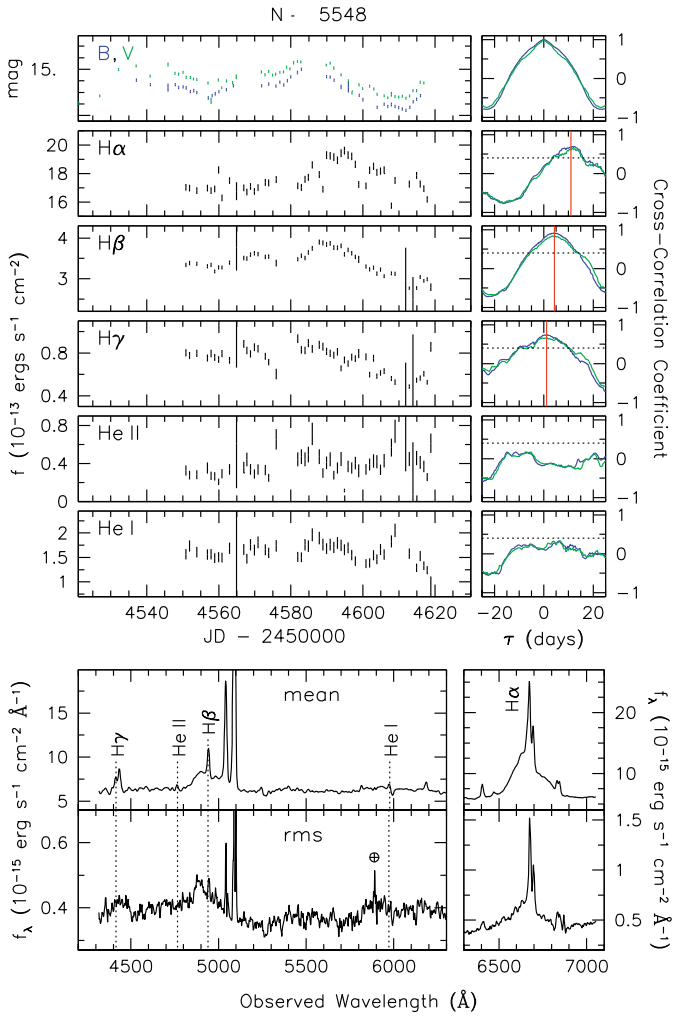

Figure 8. Same as Figure 1, but for NGC 5548.

(A color version of this figure is available in the online journal.)

in the positive direction was increased in quadrature by the difference of the corrected and uncorrected line widths. As residual narrow-line emission will always tend to bias the line-width measurement toward smaller values, the correction to the line-width uncertainties is asymmetric and only affects the uncertainty in the positive (larger line width) direction.

A further complication appears upon examination of the Hγ line in NGC 5548. This emission line is very close to the edge of the spectroscopic coverage, and in its current low-luminosity state, the broad lines in NGC 5548 are extremely broad—FWHM $\approx$ 10,000 km s^{-1} compared to only a few $\times$1000 km s^{-1} for the other objects in the sample. It is likely that the Hγ line is not fully covered by the spectral range in the LAMP data set, and as such both the mean time lag (which would only measure the response of part of the emission line) and the line width of the Hγ line in NGC 5548 are suspect.

Table 14 lists the rest-frame broad-line widths and their uncertainties. The line-width measurements for Hβ were already presented in Paper III, but we include them here for comparison with the other emission lines.

3.3. Black Hole Mass

The mass of the putative black hole is determined from the equation

$$M_{\rm BH} = f\frac{c\tau v^2}{G}, \qquad (2)$$

where τ is the mean time delay for a specific emission line, v is the velocity width of the line, c is the speed of light, and G is the gravitational constant.

The factor f in the above equation is a scaling factor of order unity that depends on the detailed geometry, kinematics, and emission processes of the line-emitting region. To date, the value of f is unknown, both for individual galaxies and the population average. Instead of adopting a value for f that is based on assuming a specific model of the BLR, we adopt the scaling factor determined in Paper IV of $\langle f\rangle \approx 5.2 \pm 1.2$, which is the value required to bring the AGN $M_{\rm BH}$–$\sigma_\star$ relationship into agreement with the local, quiescent galaxy $M_{\rm BH}$–$\sigma_\star$ relationship. This particular value of the scaling factor is based on the union of the LAMP sample and the sample previously considered by Onken et al. (2004) and is consistent with the scaling factor determined by Onken et al. (2004; $\langle f\rangle = 5.5 \pm 1.8$), which has been widely used in the literature and was used in Paper III describing the Hβ-based black hole mass derivations for this sample. Although our adopted value of f is derived for the specific case of Hβ, we will assume in the following analysis that the virial coefficient is the same for the lines discussed here. This choice is justified in the absence of observational or theoretical arguments for a varying f within the broad, optical recombination lines. As we will show, the general agreement

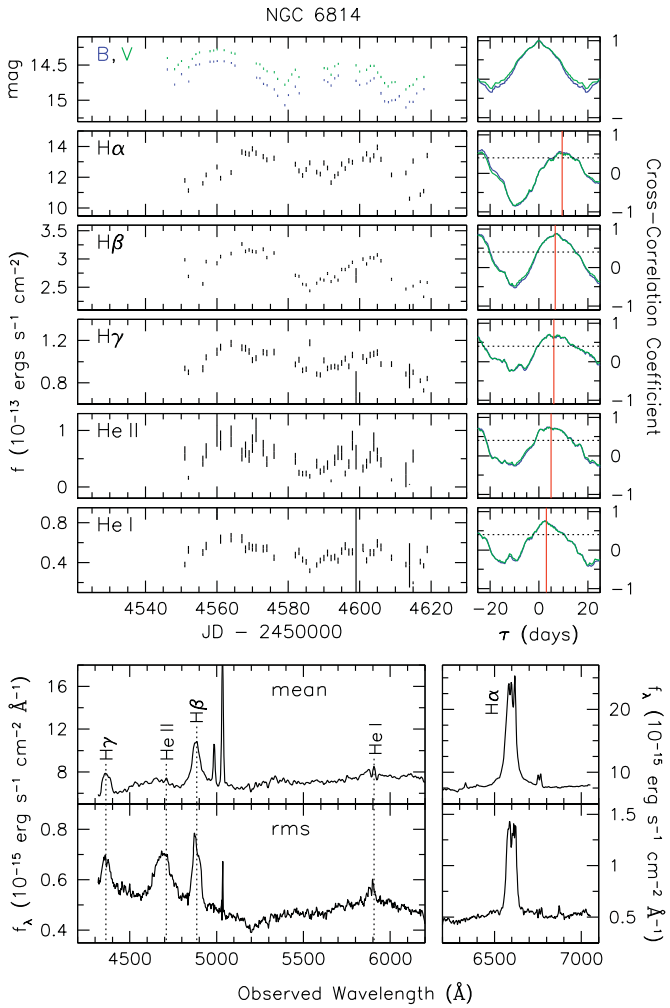

Figure 9. Same as Figure 1, but for NGC 6814.

(A color version of this figure is available in the online journal.)

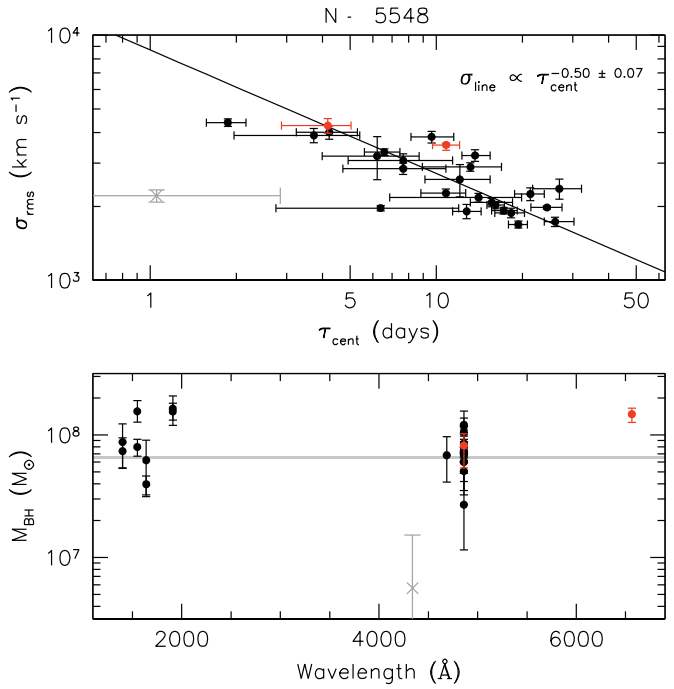

Figure 10. Top: broad emission-line width as a function of lag time for all reverberation results for NGC 5548. The solid line shows a least-squares fit to the data and has a power-law slope of −0.50, which is expected for a virial relationship. Red points are the Hα and Hβ measurements presented in this work. The gray cross is for the Hγ measurement in this work, which is unreliable and was not included in the fit. Bottom: black hole mass as a function of emission-line wavelength. The gray band shows the 1σ range of the weighted average of the black hole mass based on Hβ measurements. Symbols are as described in the top panel.

(A color version of this figure is available in the online journal.)

of virial products across the emission lines considered here confirms that this choice is appropriate.

Following the findings of Peterson et al. (2004), we use the combination of $\tau_{\rm cent}$ and $\sigma_{\rm line}$(rms) to determine the mass of the black hole in each object from each individual emission line. Table 15 lists the black hole mass calculated from each individual broad emission line for the nine objects presented in this work. We list both the "virial product," which assumes that $f = 1$, as well as the adopted black hole mass using the scaling factor from Paper IV.

4. RESULTS

4.1. Time Lag, Line Width, and M_{BH} Consistency

NGC 5548, with its many years of monitoring data, was the first AGN known to show a virial relationship between time lag and line width, indicative of the motion of BLR gas in a Keplerian potential (Peterson & Wandel 1999). In fact, this virial relationship holds for all broad optical and ultraviolet emission lines for which a time lag between the line and the continuum has been measured, as well as for all the measurements of Hβ that have been taken over some 15 years of monitoring campaigns (Bentz et al. 2007, and references therein). Several additional AGNs have since been shown to exhibit virial behavior of their broad emission lines as well, such as NGC 3738 (Onken & Peterson 2002) and Mrk 110 (Kollatschny 2003). Figure 10 (top) shows the virial relationship between lag and line width for all measured emission lines in NGC 5548 as determined by Bentz et al. (2007), with the measurements of Hα and Hβ from LAMP marked in red. The Hβ line measurements fall directly on the fitted relationship, while the Hα line measurements lie above the relationship, but within the scatter. Our earlier concerns about the Hγ line-width measurements are validated by the fact that the Hγ line measurements (marked with a gray cross) lie far away from the locus of other emission-line measurements and far below the fitted relationship. A least-squares fit (McArthur et al. 1994) to all of the time-lag and line-width measurements for NGC 5548, including the uncertainties in both time lag and line width, yields a slope of -0.50 ± 0.07, in excellent agreement with the expectation of -0.5 for a virial relationship. Comparing all of the $M_{\rm BH}$ measurements from individual emission-line reverberation results (Figure 10, bottom), we see that the mass based on Hβ falls where expected, while that of Hα is somewhat high (albeit within the scatter). The mass measurement based on the Hγ measurements presented here is extremely low and inconsistent with previous measurements.

Similar plots are presented for the other eight AGNs in Figure 11. In the left panels, we show the relationship between time lag and line width for each AGN, and the right panels show the black hole mass determined from each line. With only a small number of emission lines contributing to each plot, we do not attempt to fit a power law to the relationship between lag time and line width but instead display a power law of the form $v \propto \tau^{-0.5}$ with a dashed line to show

Table 12
Light-curve Statistics

Object (1)	Time Series (2)	N (3)	$\langle T \rangle$ (4)	$T_{\rm median}$ (5)	$\langle \sigma_{\rm f}/f \rangle$ (6)	$F_{\rm var}$ (7)	$R_{\rm max}$ (8)
Mrk 142	B	64	1.8 ± 2.3	1.02	0.0166	0.025	1.15 ± 0.03
	V	62	1.7 ± 2.0	1.02	0.0119	0.024	1.12 ± 0.02
	5100 Å	51	1.4 ± 1.0	1.00	0.0115	0.090	1.86 ± 0.03
	Hα	50	1.4 ± 1.0	1.00	0.0199	0.075	1.86 ± 0.05
	Hβ	51	1.4 ± 1.0	1.00	0.0113	0.086	1.97 ± 0.03
	Hγ	51	1.4 ± 1.0	1.00	0.0350	0.092	2.04 ± 0.10
	He II λ4686	51	1.4 ± 1.0	1.00	0.0414	0.167	2.64 ± 0.16
	He I λ5876	50	1.4 ± 1.0	1.00	0.0530	0.104	1.93 ± 0.15
SBS 1116+583A	B	56	2.1 ± 1.8	1.02	0.0205	0.104	1.63 ± 0.05
	V	56	1.9 ± 1.7	1.01	0.0220	0.082	1.47 ± 0.05
	5100 Å	50	1.4 ± 0.9	1.00	0.0437	0.043	1.36 ± 0.08
	Hα	50	1.4 ± 0.9	1.00	0.0309	0.061	1.32 ± 0.06
	Hβ	50	1.4 ± 0.9	1.00	0.0279	0.102	1.48 ± 0.06
	Hγ	50	1.4 ± 0.9	1.00	0.0410	0.129	1.90 ± 0.11
	He II λ4686	50	1.4 ± 0.9	1.00	0.1041	0.437	40.5 ± 17.0
	He I λ5876	48	1.4 ± 0.9	1.00	0.1973	0.262	7.20 ± 1.98
Arp 151	B	66	1.5 ± 1.6	1.02	0.0173	0.161	1.80 ± 0.04
	V	62	1.6 ± 1.6	1.02	0.0185	0.113	1.54 ± 0.04
	5100 Å	43	1.4 ± 1.9	1.02	0.0101	0.120	1.73 ± 0.03
	Hα	43	1.4 ± 0.9	1.02	0.0185	0.121	1.56 ± 0.04
	Hβ	43	1.4 ± 0.9	1.02	0.0153	0.169	1.74 ± 0.04
	Hγ	43	1.4 ± 0.9	1.02	0.0385	0.206	2.14 ± 0.12
	He II λ4686	43	1.4 ± 0.9	1.02	0.2396	0.623	39.0 ± 13.1
	He I λ5876	41	1.4 ± 0.9	1.02	0.1060	0.291	3.20 ± 0.50
Mrk 1310	B	50	2.0 ± 1.5	1.16	0.0160	0.116	1.71 ± 0.04
	V	58	1.8 ± 1.4	1.05	0.0183	0.073	1.39 ± 0.04
	5100 Å	47	1.5 ± 1.1	1.01	0.0367	0.051	1.44 ± 0.07
	Hα	46	1.5 ± 1.2	1.01	0.0244	0.066	1.34 ± 0.05
	Hβ	47	1.5 ± 1.1	1.01	0.0186	0.108	1.62 ± 0.04
	Hγ	47	1.5 ± 1.1	1.01	0.0301	0.077	1.40 ± 0.06
	He II λ4686	44	1.6 ± 1.2	1.01	0.3143	0.809	990 ± 2800
	He I λ5876	46	1.5 ± 1.1	1.01	0.1148	0.263	10.6 ± 2.0
Mrk 202	B	58	2.0 ± 1.7	1.01	0.0168	0.042	1.20 ± 0.03
	V	58	1.8 ± 1.7	1.01	0.0143	0.027	1.18 ± 0.04
	5100 Å	46	1.5 ± 1.2	1.01	0.0309	0.027	1.25 ± 0.05
	Hα	45	1.5 ± 1.3	1.01	0.0176	0.076	1.35 ± 0.03
	Hβ	46	1.5 ± 1.2	1.01	0.0125	0.089	1.42 ± 0.03
	Hγ	46	1.5 ± 1.2	1.01	0.0321	0.106	1.79 ± 0.08
	He II λ4686	46	1.5 ± 1.2	1.01	0.0546	0.210	2.50 ± 0.19
NGC 4253	B	51	1.9 ± 2.3	1.02	0.0066	0.032	1.16 ± 0.01
	V	54	1.8 ± 2.2	1.01	0.0046	0.028	1.15 ± 0.01
	5100 Å	50	1.4 ± 1.0	1.01	0.0180	0.053	1.31 ± 0.03
	Hα	50	1.4 ± 1.0	1.01	0.0235	0.034	1.17 ± 0.04
	Hβ	50	1.4 ± 1.0	1.01	0.0116	0.048	1.35 ± 0.15
	Hγ	49	1.4 ± 1.0	1.01	0.0376	0.051	1.74 ± 0.70
NGC 4748	B	48	2.4 ± 3.1	1.25	0.0151	0.053	1.22 ± 0.05
	V	52	2.2 ± 2.5	1.03	0.0147	0.043	1.18 ± 0.02
	5100 Å	45	1.5 ± 1.3	1.00	0.0202	0.045	1.33 ± 0.04
	Hα	45	1.5 ± 1.3	1.00	0.0221	0.067	1.38 ± 0.04
	Hβ	45	1.5 ± 1.3	1.00	0.0094	0.052	1.22 ± 0.02
	Hγ	45	1.5 ± 1.3	1.00	0.0257	0.056	1.31 ± 0.15
	He II λ4686	45	1.5 ± 1.3	1.00	0.0361	0.097	1.56 ± 0.08
NGC 5548	B	45	2.4 ± 4.3	1.07	0.0148	0.085	1.39 ± 0.03
	V	57	1.9 ± 1.8	1.05	0.0125	0.094	1.40 ± 0.02
	5100 Å	51	1.4 ± 0.9	1.01	0.0216	0.058	1.32 ± 0.04
	Hα	49	1.4 ± 0.9	1.01	0.0144	0.063	1.49 ± 0.03
	Hβ	51	1.4 ± 0.9	1.01	0.0279	0.082	1.57 ± 0.35
	Hγ	51	1.4 ± 0.9	1.01	0.1130	0.127	5.2 ± 14.2
NGC 6814	B	43	1.7 ± 1.3	1.04	0.0137	0.178	1.83 ± 0.03
	V	46	1.6 ± 1.3	1.02	0.0134	0.145	1.68 ± 0.03
	5100 Å	45	1.5 ± 1.1	1.01	0.0345	0.068	1.54 ± 0.08
	Hα	44	1.6 ± 1.1	1.01	0.0127	0.063	1.31 ± 0.02
	Hβ	45	1.5 ± 1.1	1.01	0.0124	0.093	1.58 ± 0.11
	Hγ	45	1.6 ± 1.1	1.01	0.0379	0.100	1.74 ± 0.60
	He II λ4686	42	1.7 ± 1.2	1.01	0.2370	0.419	23.7 ± 7.1
	He I λ5876	44	1.6 ± 1.1	1.01	0.0838	0.197	4.56 ± 0.46

Note. Columns are presented as follows: (1) object; (2) feature; (3) number of observations; (4) average interval (days) between observations; (5) median sampling rate (days); (6) mean fractional error; (7) excess variance as described in the text; and (8) the ratio of the maximum to the minimum flux.

Table 13
Time-lag Measurements

Object	Line	vs. *B* Band					vs. *V* Band				
		Observed		Rest Frame			Observed		Rest Frame		
		τ_{cent} (day)	τ_{peak} (day)	τ_{cent} (day)	τ_{peak} (day)	r_{max}	τ_{cent} (day)	τ_{peak} (day)	τ_{cent} (day)	τ_{peak} (day)	r_{max}
Mrk 142	Hα	$2.90^{+1.22}_{-0.92}$	$2.58^{+1.75}_{-0.50}$	$2.78^{+1.17}_{-0.88}$	$2.47^{+1.67}_{-0.48}$	0.53 ± 0.08	$2.63^{+1.24}_{-1.02}$	$2.50^{+1.50}_{-1.00}$	$2.52^{+1.18}_{-0.98}$	$2.39^{+1.44}_{-0.96}$	0.56 ± 0.08
	Hβ	$2.87^{+0.76}_{-0.87}$	$2.75^{+1.00}_{-0.75}$	$2.74^{+0.73}_{-0.83}$	$2.63^{+0.96}_{-0.72}$	0.52 ± 0.07	$2.88^{+1.00}_{-1.01}$	$3.25^{+0.75}_{-1.75}$	$2.76^{+0.96}_{-0.96}$	$3.11^{+0.72}_{-1.67}$	0.55 ± 0.08
	Hγ	$2.99^{+1.27}_{-1.10}$	$2.75^{+1.75}_{-1.00}$	$2.86^{+1.22}_{-1.05}$	$2.63^{+1.67}_{-0.96}$	0.54 ± 0.08	$3.08^{+1.55}_{-1.20}$	$3.25^{+1.50}_{-1.75}$	$2.95^{+1.48}_{-1.15}$	$3.11^{+1.44}_{-1.67}$	0.58 ± 0.07
	He II λ4686	$1.25^{+1.60}_{-2.08}$	$1.25^{+1.50}_{-2.00}$	$1.20^{+1.53}_{-1.99}$	$1.20^{+1.44}_{-1.91}$	0.50 ± 0.07	$1.61^{+1.11}_{-1.48}$	$1.50^{+1.25}_{-1.25}$	$1.54^{+1.06}_{-1.42}$	$1.44^{+1.20}_{-1.20}$	0.56 ± 0.08
	He Iλ5876	$1.89^{+2.08}_{-1.26}$	$2.00^{+2.25}_{-1.50}$	$1.81^{+1.99}_{-1.20}$	$1.91^{+2.15}_{-1.44}$	0.50 ± 0.06	$1.74^{+3.77}_{-1.61}$	$1.75^{+3.75}_{-1.50}$	$1.66^{+3.61}_{-1.54}$	$1.67^{+3.59}_{-1.44}$	0.52 ± 0.07
SBS 1116+583A	Hα	$4.12^{+1.41}_{-0.98}$	$3.75^{+1.25}_{-0.75}$	$4.01^{+1.37}_{-0.95}$	$3.65^{+1.22}_{-0.73}$	0.63 ± 0.07	$3.34^{+0.67}_{-0.85}$	$3.25^{+0.75}_{-1.00}$	$3.25^{+0.65}_{-0.83}$	$3.16^{+0.73}_{-0.97}$	0.56 ± 0.08
	Hβ	$2.38^{+0.64}_{-0.51}$	$2.25^{+1.00}_{-0.50}$	$2.31^{+0.62}_{-0.49}$	$2.19^{+0.97}_{-0.49}$	0.65 ± 0.07	$2.24^{+0.65}_{-0.61}$	$2.25^{+0.75}_{-0.50}$	$2.18^{+0.63}_{-0.60}$	$2.19^{+0.73}_{-0.49}$	0.62 ± 0.11
	Hγ	$1.89^{+0.63}_{-0.52}$	$2.00^{+0.50}_{-0.75}$	$1.84^{+0.61}_{-0.51}$	$1.95^{+0.49}_{-0.73}$	0.56 ± 0.07	$2.02^{+0.86}_{-0.62}$	$2.25^{+0.75}_{-1.00}$	$1.97^{+0.84}_{-0.60}$	$2.19^{+0.73}_{-0.97}$	0.54 ± 0.08
	He II λ4686	$0.48^{+0.40}_{-0.48}$	$0.50^{+0.25}_{-0.50}$	$0.47^{+0.39}_{-0.47}$	$0.49^{+0.24}_{-0.49}$	0.71 ± 0.07	$0.23^{+0.53}_{-0.69}$	$0.25^{+0.50}_{-0.75}$	$0.22^{+0.52}_{-0.67}$	$0.24^{+0.49}_{-0.73}$	0.66 ± 0.11
	He Iλ5876	$2.64^{+1.63}_{-2.66}$	$2.75^{+1.50}_{-3.00}$	$2.57^{+1.59}_{-2.59}$	$2.68^{+1.46}_{-2.92}$	0.52 ± 0.07	$2.14^{+1.37}_{-1.63}$	$2.25^{+1.25}_{-2.00}$	$2.08^{+1.33}_{-1.59}$	$2.19^{+1.22}_{-1.95}$	0.50 ± 0.07
Arp 151	Hα	$8.01^{+1.05}_{-1.00}$	$8.50^{+0.25}_{-1.00}$	$7.84^{+1.03}_{-0.98}$	$8.32^{+0.24}_{-0.98}$	0.92 ± 0.02	$7.49^{+1.09}_{-0.88}$	$7.75^{+1.00}_{-0.50}$	$7.34^{+1.07}_{-0.86}$	$7.59^{+0.98}_{-0.49}$	0.91 ± 0.02
	Hβ	$4.08^{+0.50}_{-0.69}$	$3.50^{+0.75}_{-0.25}$	$3.99^{+0.49}_{-0.68}$	$3.43^{+0.73}_{-0.24}$	0.971 ± 0.007	$3.52^{+0.82}_{-0.72}$	$3.50^{+1.00}_{-0.75}$	$3.45^{+0.80}_{-0.71}$	$3.43^{+0.98}_{-0.73}$	0.963 ± 0.013
	Hγ	$1.39^{+0.81}_{-0.75}$	$1.50^{+1.00}_{-1.00}$	$1.36^{+0.79}_{-0.73}$	$1.47^{+0.98}_{-0.98}$	0.934 ± 0.02	$1.04^{+0.95}_{-0.90}$	$1.25^{+1.25}_{-0.75}$	$1.02^{+0.93}_{-0.88}$	$1.22^{+1.22}_{-0.73}$	0.92 ± 0.03
	He II λ4686	$-0.69^{+1.04}_{-1.25}$	$-0.25^{+1.00}_{-0.25}$	$-0.68^{+1.02}_{-1.22}$	$-0.24^{+0.98}_{-0.24}$	0.86 ± 0.04	$-0.78^{+1.36}_{-1.49}$	$0.00^{+1.00}_{-0.75}$	$-0.76^{+1.33}_{-1.46}$	$0.00^{+0.98}_{-0.73}$	0.85 ± 0.04
	He I λ5876	$0.01^{+1.04}_{-0.86}$	$-0.25^{+2.25}_{-1.25}$	$0.01^{+1.02}_{-0.84}$	$-0.24^{+2.20}_{-1.22}$	0.90 ± 0.03	$-0.42^{+1.18}_{-1.15}$	$-0.50^{+2.00}_{-2.25}$	$-0.41^{+1.16}_{-1.13}$	$-0.49^{+1.96}_{-2.20}$	0.89 ± 0.03
Mrk 1310	Hα	$4.60^{+0.67}_{-0.62}$	$4.25^{+1.75}_{-0.75}$	$4.51^{+0.66}_{-0.61}$	$4.17^{+1.72}_{-0.74}$	0.82 ± 0.05	$4.48^{+0.65}_{-0.62}$	$4.25^{+1.25}_{-0.75}$	$4.39^{+0.64}_{-0.61}$	$4.17^{+1.23}_{-0.74}$	0.82 ± 0.05
	Hβ	$3.74^{+0.60}_{-0.62}$	$3.75^{+0.50}_{-0.50}$	$3.66^{+0.59}_{-0.61}$	$3.68^{+0.49}_{-0.49}$	0.73 ± 0.09	$3.67^{+0.46}_{-0.50}$	$3.75^{+0.50}_{-0.50}$	$3.60^{+0.45}_{-0.49}$	$3.68^{+0.49}_{-0.49}$	0.77 ± 0.07
	Hγ	$1.86^{+0.64}_{-0.72}$	$1.50^{+1.00}_{-0.25}$	$1.82^{+0.63}_{-0.71}$	$1.47^{+0.98}_{-0.25}$	0.72 ± 0.07	$1.92^{+0.59}_{-0.58}$	$1.75^{+0.75}_{-0.50}$	$1.88^{+0.58}_{-0.57}$	$1.72^{+0.74}_{-0.49}$	0.74 ± 0.07
	He II λ4686	$0.96^{+0.62}_{-0.83}$	$0.75^{+0.50}_{-0.50}$	$0.94^{+0.61}_{-0.81}$	$0.74^{+0.49}_{-0.49}$	0.63 ± 0.09	$1.10^{+0.80}_{-0.86}$	$0.75^{+1.50}_{-0.75}$	$1.08^{+0.78}_{-0.84}$	$0.74^{+1.47}_{-0.74}$	0.63 ± 0.08
	He Iλ5876	$2.61^{+0.92}_{-1.08}$	$2.50^{+1.00}_{-1.25}$	$2.56^{+0.90}_{-1.05}$	$2.45^{+0.98}_{-1.23}$	0.63 ± 0.08	$2.39^{+0.98}_{-0.97}$	$2.50^{+0.50}_{-1.00}$	$2.34^{+0.96}_{-0.95}$	$2.45^{+0.49}_{-0.98}$	0.64 ± 0.08
Mrk 202	Hα	$:22.35^{+1.28}_{-3.80}$	$:22.00^{+2.25}_{-2.50}$	$:21.89^{+1.25}_{-3.72}$	$:21.55^{+2.20}_{-2.45}$	0.77 ± 0.06	$:14.52^{+7.83}_{-10.47}$	$:14.75^{+7.50}_{-10.75}$	$:14.22^{+7.66}_{-10.26}$	$:14.45^{+7.35}_{-10.53}$	0.62 ± 0.08
	Hβ	$3.12^{+1.77}_{-1.15}$	$3.00^{+1.50}_{-1.25}$	$3.05^{+1.73}_{-1.12}$	$2.94^{+1.47}_{-1.22}$	0.80 ± 0.05	$3.11^{+0.91}_{-1.12}$	$2.75^{+1.75}_{-1.25}$	$3.05^{+0.89}_{-1.10}$	$2.69^{+1.71}_{-1.22}$	0.70 ± 0.07
	Hγ	$3.38^{+1.60}_{-1.41}$	$3.50^{+1.50}_{-2.00}$	$3.31^{+1.57}_{-1.38}$	$3.43^{+1.47}_{-1.96}$	0.68 ± 0.06	$3.49^{+16.57}_{-3.06}$	$3.56^{+16.50}_{-3.25}$	$3.42^{+16.23}_{-3.00}$	$3.49^{+16.16}_{-3.18}$	0.64 ± 0.07
	He II λ4686	$1.50^{+2.45}_{-1.22}$	$0.50^{+2.75}_{-1.00}$	$1.47^{+2.40}_{-1.19}$	$0.49^{+2.69}_{-0.98}$	0.78 ± 0.05	$1.89^{+16.99}_{-1.63}$	$1.75^{+17.00}_{-2.00}$	$1.85^{+16.64}_{-1.60}$	$1.71^{+16.65}_{-1.96}$	0.67 ± 0.08
NGC 4253	Hα	$25.50^{+0.66}_{-0.86}$	$25.75^{+0.50}_{-1.00}$	$25.17^{+0.65}_{-0.85}$	$25.42^{+0.49}_{-0.99}$	0.53 ± 0.08	$25.12^{+1.50}_{-0.87}$	$25.25^{+1.50}_{-1.25}$	$24.80^{+1.48}_{-0.86}$	$24.93^{+1.48}_{-1.23}$	0.54 ± 0.07
	Hβ	$6.24^{+1.65}_{-1.24}$	$6.00^{+2.50}_{-1.00}$	$6.16^{+1.63}_{-1.22}$	$5.92^{+2.47}_{-0.99}$	0.59 ± 0.09	$6.87^{+1.22}_{-1.84}$	$6.50^{+2.25}_{-2.00}$	$6.78^{+1.20}_{-1.81}$	$6.42^{+2.22}_{-1.97}$	0.68 ± 0.08
	Hγ	$6.86^{+2.38}_{-3.27}$	$6.50^{+2.75}_{-3.00}$	$6.78^{+2.35}_{-3.23}$	$6.42^{+2.71}_{-2.96}$	0.58 ± 0.08	$8.40^{+1.76}_{-4.67}$	$8.50^{+1.75}_{-4.75}$	$8.29^{+1.74}_{-4.60}$	$8.39^{+1.73}_{-4.69}$	0.61 ± 0.09
NGC 4748	Hα	$7.61^{+3.01}_{-4.64}$	$8.50^{+1.75}_{-6.25}$	$7.50^{+2.97}_{-4.57}$	$8.38^{+1.72}_{-6.16}$	0.71 ± 0.07	$10.84^{+3.07}_{-3.05}$	$10.75^{+4.00}_{-2.00}$	$10.68^{+3.03}_{-2.92}$	$10.59^{+3.94}_{-1.91}$	0.70 ± 0.08
	Hβ	$5.63^{+1.64}_{-2.25}$	$5.75^{+3.50}_{-2.00}$	$5.55^{+1.62}_{-2.22}$	$5.67^{+3.45}_{-1.97}$	0.81 ± 0.05	$6.39^{+1.84}_{-1.46}$	$7.75^{+1.75}_{-3.75}$	$6.30^{+1.82}_{-1.44}$	$7.64^{+1.72}_{-3.70}$	0.77 ± 0.05
	Hγ	$7.02^{+2.64}_{-3.27}$	$7.75^{+2.25}_{-3.50}$	$6.92^{+2.60}_{-3.22}$	$7.64^{+2.22}_{-3.45}$	0.72 ± 0.06	$7.09^{+3.66}_{-4.57}$	$7.50^{+3.25}_{-6.00}$	$6.99^{+3.61}_{-4.37}$	$7.39^{+3.20}_{-5.73}$	0.70 ± 0.06
	He II λ4686	$1.02^{+7.92}_{-1.39}$	$0.75^{+8.00}_{-1.00}$	$1.00^{+7.80}_{-1.37}$	$0.74^{+7.88}_{-0.99}$	0.78 ± 0.06	$0.95^{+3.66}_{-1.33}$	$0.50^{+5.00}_{-0.75}$	$0.93^{+3.61}_{-1.27}$	$0.49^{+4.93}_{-0.72}$	0.76 ± 0.06
NGC 5548	Hα	$11.02^{+1.27}_{-1.15}$	$11.50^{+1.25}_{-2.00}$	$10.83^{+1.24}_{-1.13}$	$11.31^{+1.23}_{-1.97}$	0.71 ± 0.06	$11.65^{+0.83}_{-1.51}$	$11.50^{+1.75}_{-1.25}$	$11.45^{+0.82}_{-1.49}$	$11.31^{+1.72}_{-1.23}$	0.65 ± 0.07
	Hβ	$4.25^{+0.88}_{-1.33}$	$4.25^{+1.25}_{-1.50}$	$4.18^{+0.86}_{-1.30}$	$4.18^{+1.23}_{-1.47}$	0.86 ± 0.07	$4.24^{+0.91}_{-1.35}$	$4.25^{+1.50}_{-1.25}$	$4.17^{+0.90}_{-1.33}$	$4.18^{+1.47}_{-1.23}$	0.80 ± 0.08
	Hγ	$:1.25^{+1.86}_{-2.33}$	$:1.00^{+1.50}_{-2.50}$	$:1.23^{+1.83}_{-2.29}$	$:0.98^{+1.47}_{-2.46}$	0.71 ± 0.08	$:1.49^{+1.98}_{-3.33}$	$:0.75^{+3.75}_{-3.00}$	$:1.47^{+1.95}_{-3.27}$	$:0.74^{+3.69}_{-2.95}$	0.66 ± 0.09
NGC 6814	Hα	$9.51^{+1.91}_{-1.56}$	$9.25^{+2.75}_{-1.25}$	$9.46^{+1.90}_{-1.56}$	$9.20^{+2.74}_{-1.24}$	0.60 ± 0.08	$9.62^{+2.25}_{-1.73}$	$9.25^{+2.75}_{-1.50}$	$9.57^{+2.23}_{-1.72}$	$9.20^{+2.74}_{-1.49}$	0.57 ± 0.08
	Hβ	$6.67^{+0.88}_{-0.90}$	$7.25^{+0.25}_{-0.75}$	$6.64^{+0.87}_{-0.90}$	$7.21^{+0.25}_{-0.75}$	0.87 ± 0.04	$6.49^{+0.95}_{-0.96}$	$7.00^{+0.50}_{-0.50}$	$6.46^{+0.94}_{-0.96}$	$6.96^{+0.50}_{-0.50}$	0.86 ± 0.04
	Hγ	$6.08^{+2.66}_{-2.35}$	$5.25^{+3.50}_{-1.25}$	$6.05^{+2.65}_{-2.34}$	$5.22^{+3.48}_{-1.24}$	0.71 ± 0.09	$6.14^{+2.21}_{-2.24}$	$6.25^{+2.00}_{-2.25}$	$6.11^{+2.20}_{-2.23}$	$6.22^{+1.99}_{-2.24}$	0.72 ± 0.08
	He II λ4686	$5.03^{+1.99}_{-1.84}$	$4.25^{+3.75}_{-1.75}$	$5.00^{+1.98}_{-1.83}$	$4.23^{+3.73}_{-1.74}$	0.73 ± 0.07	$4.89^{+2.13}_{-2.03}$	$4.25^{+3.25}_{-2.75}$	$4.86^{+2.12}_{-2.02}$	$4.23^{+3.23}_{-2.74}$	0.72 ± 0.08
	He I λ5876	$3.11^{+1.33}_{-0.84}$	$2.50^{+1.75}_{-0.75}$	$3.09^{+1.33}_{-0.84}$	$2.49^{+1.74}_{-0.75}$	0.70 ± 0.10	$2.98^{+1.28}_{-0.88}$	$2.50^{+1.50}_{-0.75}$	$2.96^{+1.27}_{-0.88}$	$2.49^{+1.49}_{-0.75}$	0.70 ± 0.11

Notes. Hβ lags were first presented in Paper III and are included here for reference. Lag values preceded by a colon are considered unreliable (see the text for details).

the expected behavior for a virial relationship. In general, most objects are consistent with exhibiting virial behavior. NGC 4253 is perhaps the least consistent, but the data quality for NGC 4253 is rather low given the weak variability in the AGN during our monitoring campaign. In addition, we only have measurements for three emission lines, so the inconsistency is not surprising. In the right panels, we show the black hole mass as a function of emission-line wavelength. Gray bands show the range allowed by the 1σ uncertainties in the black hole mass determined from the Hβ line (our most well-calibrated emission line) for comparison with the black hole mass determinations from other lines. Again, the results are generally consistent within a particular object except for NGC 4253, but the black hole mass is simply a combination of the line width and lag time, for which we have somewhat poor measurements in this object.

Table 14
Rest-frame Broad Emission-line-width Measurements

Object	Line	Mean Spectrum		rms Spectrum	
		$\sigma_{\rm line}$ (km s^{-1})	FWHM (km s^{-1})	$\sigma_{\rm line}$ (km s^{-1})	FWHM (km s^{-1})
Mrk 142	Hα	925 ± 38	1350 ± 39	934 ± 61	1262 ± 166
	Hβ	1116 ± 22	1462 ± 2	859 ± 102	1368 ± 379
	Hγ	1114 ± 67	1889 ± 69	1057 ± 82	2547 ± 533
	He II λ4686	...	...	3079 ± 166	8061 ± 1325
	He Iλ5876	...	...	1128 ± 241	5703 ± 3440
SBS 1116+583A	Hα	1250^{+50}_{20}	$2059^{+508}_{-16}>$	1218^{+147}_{-99}	1965^{1408}_{374}
	Hβ	1552 ± 36	3668 ± 186	1528 ± 184	3604 ± 1123
	Hγ	1084 ± 33	3877 ± 98	1402 ± 95	4241 ± 1465
	He II λ4686	...	...	2355 ± 125	5823 ± 930
	He Iλ5876	...	...	1786 ± 137	4764 ± 1648
Arp 151	Hα	1367 ± 11	1852 ± 7	937 ± 34	1859 ± 142
	Hβ	2006 ± 24	3098 ± 69	1252 ± 46	2357 ± 142
	Hγ	1228 ± 31	3108 ± 13	1412 ± 76	3210 ± 200
	He II λ4686	...	...	2220 ± 106	6000 ± 865
	He I λ5876	...	...	1986 ± 178	3784 ± 1080
Mrk 1310	Hα	887^{+111}_{-18}	561^{+950}_{-136}	717 ± 75	677 ± 225
	Hβ	1209 ± 42	2409 ± 24	755 ± 138	1602 ± 250
	Hγ	958 ± 49	2428 ± 317	842 ± 89	2204 ± 528
	He II λ4686	...	...	1851 ± 106	4704 ± 3588
	He I λ5876	...	...	1399 ± 151	4826 ± 1625
Mrk 202	Hα	746^{+109}_{-9}	463^{+655}_{-38}	734 ± 22	663 ± 201
	Hβ	867 ± 40	1471 ± 18	659 ± 65	1354 ± 250
	Hγ	998 ± 74	2212 ± 366	1185 ± 131	1517 ± 564
	He II λ4686	...	...	1988 ± 80	3585 ± 1017
NGC 4253	Hα	801^{+60}_{-5}	1013 ± 15	726 ± 35	901 ± 150
	Hβ	1088 ± 37	1609 ± 39	516 ± 218	834 ± 1260
	Hγ	986 ± 29	2778 ± 92	1259 ± 322	3008 ± 2053
NGC 4748	Hα	901^{+46}_{-15}	1967^{+10}_{-906}	1035 ± 74	1605 ± 117
	Hβ	1009 ± 27	1947 ± 66	657 ± 91	1212 ± 173
	Hγ	925 ± 40	1617 ± 58	908 ± 148	1969 ± 715
	He II λ4686	...	...	1897 ± 193	3948 ± 1310
NGC 5548	Hα	3540^{+51}_{-25}	1643^{+3103}_{-12}	3562^{+67}_{-175}	1559^{+6090}_{-140}
	Hβ	4266 ± 65	12771 ± 71	4270 ± 292	11177 ± 2266
	Hγ	: 845 ± 29	: 2374 ± 34	: 2210 ± 126	: 5517 ± 2560
NGC 6814	Hα	1686 ± 29	2909 ± 3	1082 ± 52	2827 ± 62
	Hβ	1918 ± 36	3323 ± 7	1610 ± 108	3277 ± 297
	Hγ	1143 ± 10	3790 ± 72	1260 ± 127	3340 ± 636
	He II λ4686	...	...	2585 ± 137	6017 ± 745
	He I λ5876	...	...	3262 ± 1137	6436 ± 1342

Notes. Hβ line widths were first presented in Paper III and are included here for reference. Line widths preceded by a colon are considered unreliable (see the text for details).

4.2. Velocity-resolved Lag Measurements

Reverberation mapping seeks to fully map out the response of the line-emitting gas in the BLR as a function of both time and velocity. In Paper III, we describe the expected behavior of three simple kinematic models of the BLR (pure radial infall, ballistic outflow, and circular orbits in a Keplerian potential) with the same geometric and radiation parameters for each model (see Figure 10 of Paper III for a visual presentation of the expected responses across the line profile). In the case of circular orbits, the lag time as a function of velocity is symmetric about the line center and could even appear flat across the emission line depending on the physical details of the BLR. Both infall and outflow show asymmetric behavior, with infall having longer lags at blueshifted (negative) velocities and shorter lags at redshifted (positive) velocities. For outflow, the opposite is expected.

In Paper III, we present velocity-resolved lag times measured across the Hβ emission-line profile for six of our objects—SBS 1116+583A, Arp 151 (first presented in Paper I), Mrk 1310, NGC 4748, NGC 5548, and NGC 6814. Using the same techniques outlined there and in Section 3.1, for these six objects we divided both the Hα and Hγ lines into four velocity bins of equal variable flux and calculated the average lag time for each velocity bin relative to the *B*-band light curve. Attempts to do the same for the He II and He I lines showed no difference in lag measurements as a function of velocity. We describe the results for the Balmer lines for each of the individual objects below.

SBS 1116+583A. The Hβ velocity-resolved lags for SBS 1116 clearly show a symmetric pattern about zero velocity, with shorter lags in the wings and longer lags at the line center, indicative of circular orbits. The same pattern can easily be seen in the Hα and Hγ lines (see Figure 12). In addition, the Hγ line

Table 15
Virial Products and Derived Black Hole Masses

Object	Line	$c\tau_{\rm cent}\sigma^2_{\rm line}/G$ ($10^6\ M_\odot$)	$M_{\rm BH}$[a] ($10^6\ M_\odot$)
Mrk 142	Hα	$0.47^{+0.21}_{-0.16}$	$2.48^{+1.09}_{-0.85}$
	Hβ	$0.40^{+0.14}_{-0.15}$	$2.07^{+0.74}_{-0.80}$
	Hγ	$0.62^{+0.28}_{-0.25}$	$3.3^{+1.5}_{-1.3}$
	He II λ4686	$2.2^{+2.8}_{-3.7}$	12^{+15}_{-19}
	He Iλ5876	$0.45^{+0.53}_{-0.36}$	$2.4^{+2.8}_{-1.9}$
SBS 1116+583A	Hα	$1.16^{+0.49}_{-0.33}$	$6.1^{+2.5}_{-1.8}$
	Hβ	$1.05^{+0.38}_{-0.34}$	$5.5^{+2.0}_{-1.8}$
	Hγ	$0.71^{+0.25}_{-0.22}$	$3.7^{+1.3}_{-1.1}$
	He II λ4686	$0.51^{+0.43}_{-0.50}$	$2.7^{+2.2}_{-2.6}$
	He I λ5876	$1.6^{+1.0}_{-1.6}$	$8.8^{+5.6}_{-9.0}$
Arp 151	Hα	$1.34^{+0.20}_{-0.19}$	$7.0^{+1.1}_{-1.0}$
	Hβ	$1.22^{+0.17}_{-0.23}$	$6.41^{+0.92}_{-1.19}$
	Hγ	$0.53^{+0.31}_{-0.29}$	$2.8^{+1.6}_{-1.5}$
Mrk 1310	Hα	$0.45^{+0.12}_{-0.11}$	$2.38^{+0.61}_{-0.59}$
	Hβ	$0.41^{+0.16}_{-0.16}$	$2.14^{+0.86}_{-0.86}$
	Hγ	$0.25^{+0.10}_{-0.11}$	$1.33^{+0.54}_{-0.59}$
	He II λ4686	$0.63^{+0.41}_{-0.55}$	$3.3^{+2.2}_{-2.9}$
	He I λ5876	$0.98^{+0.40}_{-0.45}$	$5.1^{+2.1}_{-2.4}$
Mrk 202	Hα	$:2.30^{+0.19}_{-0.42}$	$:12.1^{+1.0}_{-2.2}$
	Hβ	$0.26^{+0.16}_{-0.11}$	$1.36^{+0.82}_{-0.57}$
	Hγ	$0.32^{+0.21}_{-0.18}$	$1.70^{+1.12}_{-0.95}$
	He II λ4686	$1.13^{+1.85}_{-0.93}$	$5.9^{+9.7}_{-4.9}$
NGC 4253	Hα	$2.59^{+0.26}_{-0.27}$	$13.6^{+1.4}_{-1.4}$
	Hβ	$0.32^{+0.28}_{-0.25}$	$1.7^{+1.5}_{-1.3}$
	Hγ	$2.1^{+1.3}_{-1.5}$	$11.0^{+6.8}_{-7.7}$
NGC 4748	Hα	$1.57^{+0.66}_{-0.98}$	$8.2^{+3.5}_{-5.2}$
	Hβ	$0.47^{+0.19}_{-0.23}$	$2.5^{+1.0}_{-1.2}$
	Hγ	$1.11^{+0.55}_{-0.63}$	$5.8^{+2.9}_{-3.3}$
	He II λ4686	$0.70^{+5.48}_{-0.97}$	4^{+29}_{-5}
NGC 5548	Hα	$26.8^{+3.2}_{-3.9}$	141^{+17}_{-20}
	Hβ	$14.9^{+3.7}_{-5.1}$	78^{+19}_{-27}
	Hγ	$:1.2^{+1.7}_{-2.2}$	$:6.2^{+9.2}_{-11.5}$
NGC 6814	Hα	$2.16^{+0.48}_{-0.41}$	$11.3^{+2.5}_{-2.2}$
	Hβ	$3.36^{+0.63}_{-0.64}$	$17.6^{+3.3}_{-3.4}$
	Hγ	$1.88^{+0.90}_{-0.82}$	$9.8^{+4.7}_{-4.3}$
	He II λ4686	$6.5^{+2.7}_{-2.5}$	34^{+14}_{-13}
	He I λ5876	$6.4^{+5.3}_{-4.8}$	34^{+27}_{-25}

Notes. Hβ-based masses were first presented in Paper III and are included here for reference. Values preceded by a colon are considered unreliable (see the text for details).

[a] Assuming $f = 5.2$, from Woo et al. (2010). Note that the derived masses would increase by ~5% using $f = 5.5$ from Onken et al. (2004).

seems to show a double-peaked profile, an indication of flattened geometry within the BLR gas. Comparison of the Hβ and Hγ lines reveals the possibility that the Hβ variable emission is also double peaked, with the stronger peak on the redshifted side as is seen in Hγ. The strong residuals from the narrow Hα and [N II] lines superimposed on the variable broad Hα emission do not allow a visual comparison of the variable Hα profile with those of Hβ and Hγ. Finally, the Hγ variable emission is somewhat blueshifted relative to the mean line profile.

Arp 151. First described in Paper I, the velocity-resolved Hβ emission has a strongly asymmetric lag behavior across the line profile. The blueshifted emission has long lag times that are higher than the total mean lag time, while the redshifted emission drops off to almost zero lag in the high-velocity gas in the wings. This seems to imply simple inflow in the BLR of Arp 151. Comparison with the velocity-resolved lags measured for the Hα and Hγ lines in Figure 13 shows similar behavior, again emphasizing the strong red–blue asymmetry in the emission-line responses. The variable line profiles appear to be single-peaked and do not in general show a large velocity offset from the mean line profile, although there seems to be excess emission in the red wing of each line.

Mrk 1310. While the Hβ velocity-resolved lags for Mrk 1310 exhibit a symmetric behavior about zero velocity, the Hα and Hγ velocity-resolved structure is not so orderly, as shown in Figure 14. Rather, the Hγ line seems to exhibit evidence for outflow with a slight red–blue lag asymmetry, and the variable line profile for Hγ is highly blueshifted from the mean line profile. The variable emission in Hα and Hβ, on the other hand, does not show a strong velocity shift relative to the mean emission-line profiles. More detailed analysis is clearly needed to disentangle the BLR behavior of Mrk 1310, but the consistency with a flat response across the line profile may argue for circular orbits in a Keplerian potential.

NGC 4748. As described in Paper III, the Hβ velocity-resolved lags in NGC 4748 (Figure 15) may show evidence for outflow with an asymmetric response about zero velocity. The behavior of the velocity-resolved lags within Hα and Hγ, however, is not clear at all. With the rather large uncertainties for this object, the behavior is consistent with a flat response across the emission lines, which would be consistent with circular orbits in a Keplerian potential. While the Hα variable emission shows no evidence for a large velocity shift, the Hβ variable emission shows a slight blueshift relative to the mean line profile, and the Hγ variable emission is highly blueshifted. There also appears to be excess blue-wing emission in the variable flux of each Balmer line.

NGC 5548. The Hβ velocity-resolved lag behavior for NGC 5548 is not particularly enlightening, and unfortunately, neither is that of Hα nor Hγ (see Figure 16). The overall behavior appears to be consistent with a flat response across the line profile, which could be consistent with circular orbits in a Keplerian potential. We have previously mentioned several reasons why the Hγ line in this particular data set for NGC 5548 may not be reliable. Given its shorter lag time, we would expect the Hγ line to be broader than Hα and Hβ. Instead, it appears that we may be missing a relatively large fraction of the Hγ emission at the blue end, where the spectral coverage cuts off. For this reason as well as those previously mentioned, we will classify the Hγ measurements included in this work as "unreliable."

NGC 6814. Similar to SBS 1116, the velocity-resolved lags across the Hβ emission profile of NGC 6814 show a symmetric behavior. This symmetric behavior is also seen in the Hα and Hγ lines (see Figure 17). All three emission lines seem to have a double-peaked profile shape in the variable emission, possibly indicative of a disk-like geometry in the BLR. There does not appear to be any significant velocity shift in the variable emission compared to the mean line profiles, and the widths of the variable and mean profiles are very similar, demonstrating that the full range of gas giving rise to the integrated line flux is responding to changes in the continuum flux.

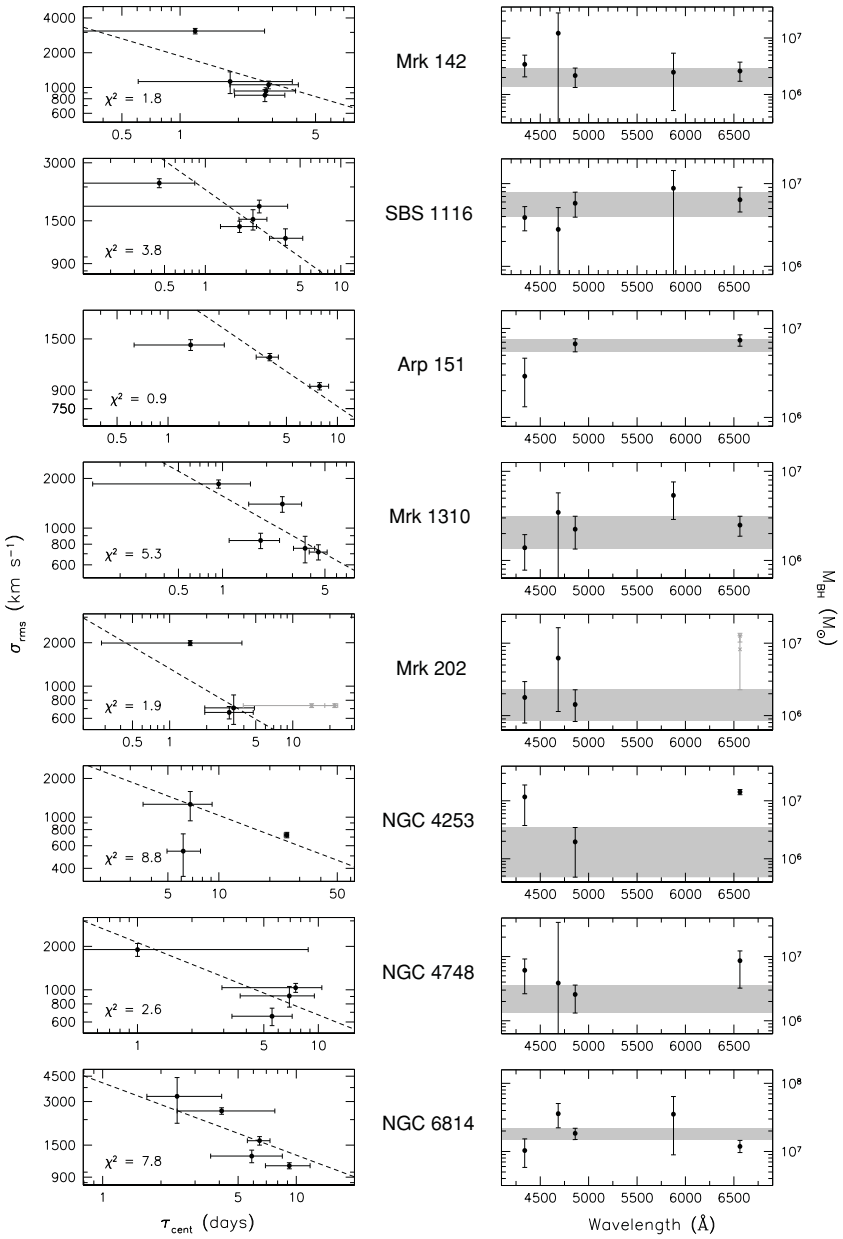

Figure 11. Left: broad emission-line width as a function of lag time for the other eight LAMP targets. The dashed line shows a power-law slope of −0.5, which is expected for a virial relationship. The gray crosses in the Mrk 202 plot show the unreliable Hα measurements for that object. Right: black hole mass as a function of emission-line wavelength. The gray band shows the 1σ range of black hole mass based on the measurements from the Hβ line, which is the most accurately calibrated broad line in the LAMP spectra. Symbols are as described for the left panels.

4.3. Comparison with Photoionization Predictions

With the large number of optical emission lines (∼5) for which we have carried out a reverberation-mapping analysis in each object, we are able to examine and compare the behavior of trends that are exhibited among emission lines with predictions from photoionization calculations of BLR-like gas. Here, we focus on the specific predictions for the optical recombination lines presented by Korista & Goad (2004). Their predictions are based on a grid of photoionization calculations, originally presented by Korista & Goad (2000), and generated with CLOUDY (Ferland et al. 1998) to model the broad UV emission lines in NGC 5548.

Among the Balmer lines, we find a trend of $\tau(\mathrm{H}\alpha) > \tau(\mathrm{H}\beta) > \tau(\mathrm{H}\gamma)$. This trend is seen in other monitoring studies of multiple AGNs (e.g., Kaspi et al. 2000), but it has not been particularly significant in previous studies due to the large uncertainties in the time-lag measurements. Under pure recombination, the emission from all the Balmer lines would be expected to originate from the same location in the BLR. However, it has long been known that an additional process beyond recombination must be affecting the observed behavior of the broad Balmer lines in AGNs, as evidenced by a variable Balmer decrement (e.g., Peterson & Ferland 1986; Cohen et al. 1986). The modification of pure recombination effects is theorized to be the result of radial stratification of optical-depth effects within the BLR (e.g., Netzer 1975; Rees et al. 1989; Korista & Goad 2004). In essence, the gas densities of the line-emitting "clouds" are higher at smaller radii (closer to the black hole), so the relative-flux variations are strongly weighted by gas at larger radii where

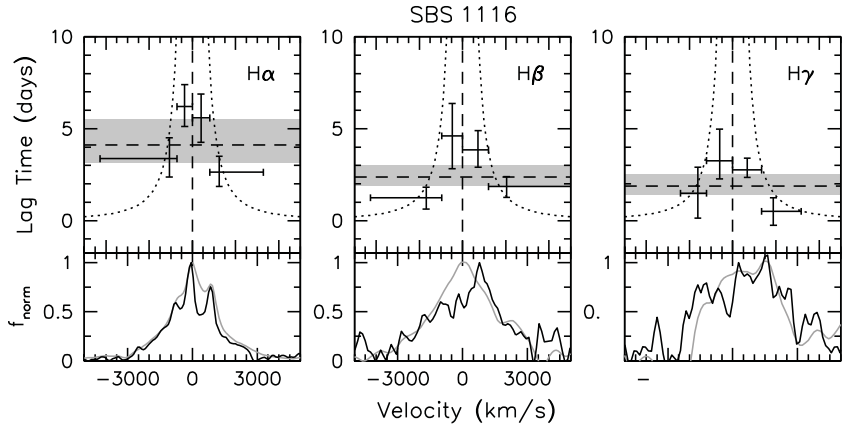

Figure 12. Top: velocity-resolved lag measurements for the broad Balmer line emission in SBS 1116. The dashed line and gray band display the average time lag and the 1σ uncertainty, respectively, for each emission line. The dotted curve in each panel is the Keplerian envelope for the adopted virial product based on the Hβ time-lag and line-width measurements. Bottom: black lines show the normalized variable (rms) Balmer emission-line profiles, while the gray lines show the normalized mean emission-line profiles for comparison.

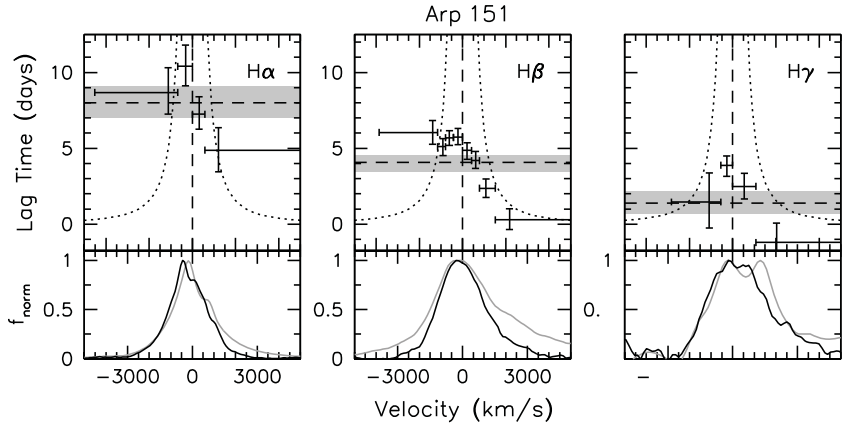

Figure 13. Same as Figure 12, but for Arp 151.

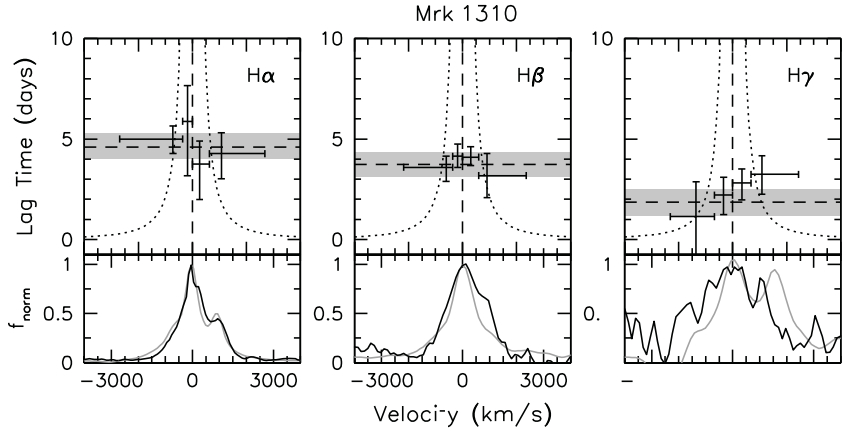

Figure 14. Same as Figure 12, but for Mrk 1310.

the densities and optical depths to line emission are smaller. This, together with the fact that at a given continuum flux, the optical depth of Hα is largest, followed by Hβ, and so on through the Balmer series, will serve to make the emission from each of these lines appear to originate at a different distance from the source (see Figure 3 of Korista & Goad 2004), with the Hα emission appearing to originate at the largest radius (i.e., largest mean time delay). The optical depths of He Iλ5876 and He II λ4686 are even smaller than those of the Balmer lines, with that of He II being the smallest of all the lines considered here, causing their responsivity-weighted radii to be even smaller, as we indeed see. For all of the "reliable" lags measured here, the weighted average time-lag ratios are τ(Hα):τ(Hβ):τ(Hγ):τ(He I):τ(He II) = 1.54:1.00:0.61:0.36:0.25 (see Figure 18).

The responsivity of the lines within a specific AGN can also be compared, where the responsivity (η) of an emission line is a measure of the efficiency of the BLR gas in converting a *change* in ionizing flux to line flux. Examination of the

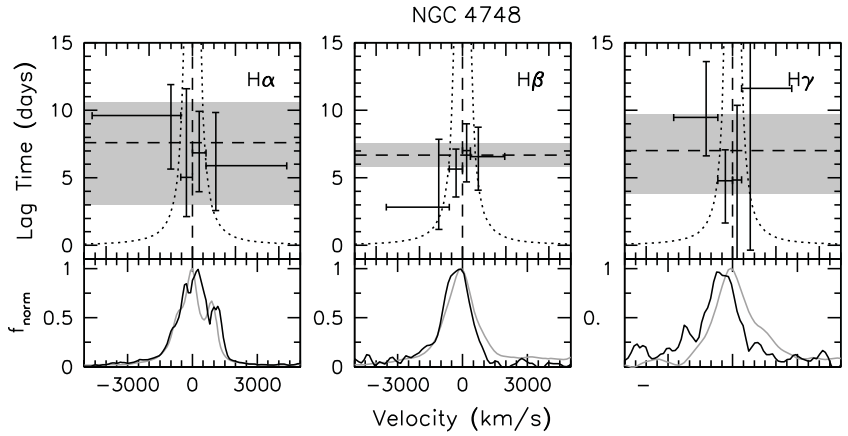

Figure 15. Same as Figure 12, but for NGC 4748.

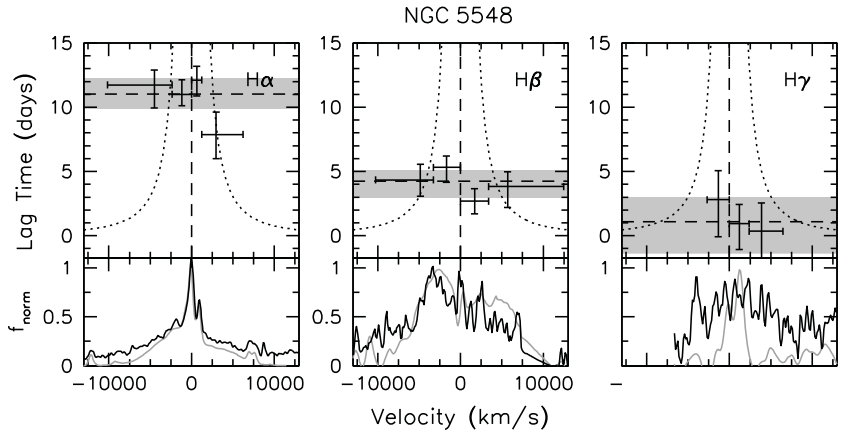

Figure 16. Same as Figure 12, but for NGC 5548.

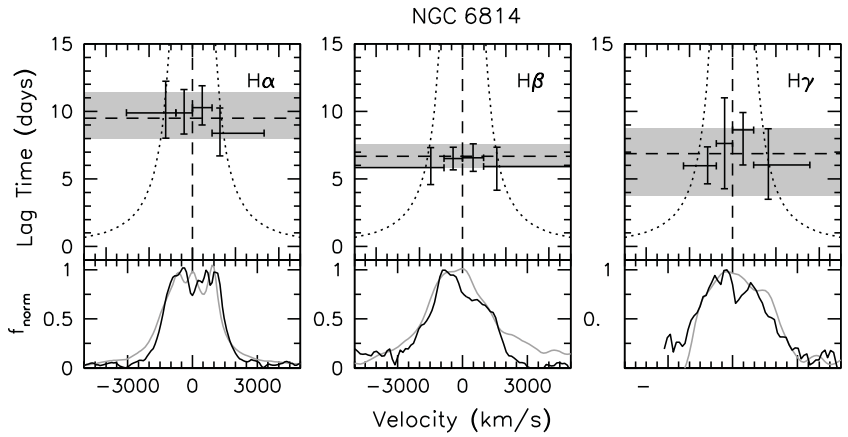

Figure 17. Same as Figure 12, but for NGC 6814.

values $F_{\rm var}$ and $R_{\rm max}$ in Table 12 shows that, in general, η(He II)> η(He I)> $\eta(\mathrm{H}\gamma) > \eta(\mathrm{H}\beta) > \eta(\mathrm{H}\alpha)$ (see Figure 18). Comparison of the light curves in Figures 1–9 also illustrates that proportionally larger variations are seen in the He lines than the Balmer lines, in response to changes in the continuum flux. This trend is in keeping with the predictions of Korista & Goad (2004) and the findings of previous monitoring programs (e.g., Peterson & Ferland 1986; Dietrich et al. 1993; Kollatschny 2003).

Finally, we find here that the line width measured in the variable part of the spectrum is typically narrower than the line width measured in the mean spectrum. This trend has been seen in most previous monitoring programs (see Peterson et al. 2004) and is another prediction that naturally arises from the photoionization calculations of Korista & Goad (2004). The expectation is that the outer wings of the lines are generated in the inner BLR, where the gas velocities are high. However, the ionization is also higher in the inner BLR, and the gas responsivity is therefore lower. Hence, the variability of the wings of the emission lines will be much lower than that of the line cores, causing the variable part of the emission line to appear narrower.

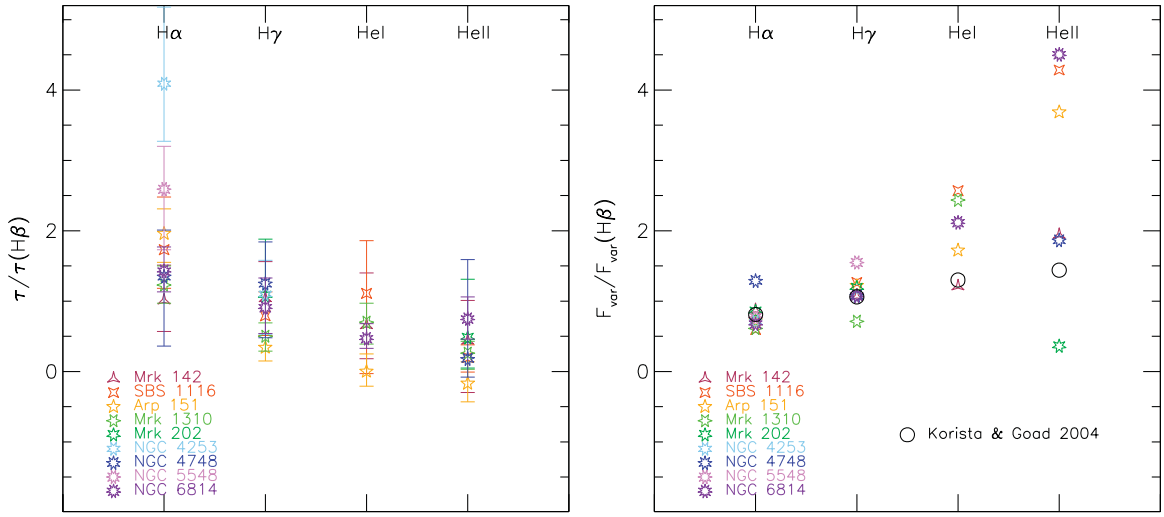

Figure 18. Left: ratio of the time delay relative to that of Hβ for each of the objects and emission lines examined here. The weighted mean ratios are found to be τ(Hα):τ(Hβ):τ(Hγ):τ(He I):τ(He II) = 1.54:1.00:0.61:0.36:0.25. This is in the same direction as the trend predicted by Korista & Goad (2004) for the responsivity-weighted radius of emission for the optical recombination lines. Right: ratio of the excess variance relative to that of Hβ for each of the objects and emission lines examined here. The open black circles show the predicted emission-line responsivity relative to that of Hβ as tabulated by Korista & Goad (2004). The trend seen here of η(He II)> η(He I)> η(Hγ) > η(Hβ) > η(Hα) is in the same direction as that predicted by Korista & Goad, although the observed trend is a bit steeper than predicted.

(A color version of this figure is available in the online journal.)

5. CONCLUSIONS

The LAMP sample of AGNs was originally chosen for spectroscopic monitoring in order to extend to lower masses the range of black hole scaling relationships in AGNs. With the high-quality spectroscopic data set obtained at Lick Observatory, we are able to go beyond the original goals of LAMP and begin to examine the details of the BLR physics in these AGNs in the following ways.

1. We have presented time-delay measurements and line widths for all of the optical H and He recombination lines in the spectra of the LAMP sample of AGNs: Hα, Hβ, Hγ, He II λ4686, and He I λ5876.
2. Comparisons of the black hole masses determined from multiple emission lines are consistent within individual sources, even when assuming a single scaling factor f. For at least the optical recombination lines, it appears that the scaling factor is not heavily dependent on the specific emission line when determining black hole masses from reverberation mapping.
3. The time-lag versus the line-width measurements for multiple emission lines in an individual source are generally consistent with a virial relationship ($\tau \propto v^{-2}$). Virial relationships have been seen in other AGNs with high-quality spectroscopic monitoring data, upholding the use of reverberation-mapping results as a probe of the gravitational influence of the supermassive black hole on the BLR gas.
4. For six of the LAMP AGNs, we have examined the velocity-resolved time-lag response across the broad Hα, Hβ, and Hγ lines. In three of the AGNs, we find a significant trend in the delay versus the velocity across the line profiles of all three Balmer lines. In the other three AGNs, there is no significant trend in delay across the line profile, which may, in fact, argue for evidence of circular motions in a Keplerian potential. We are currently investigating whether more detailed decompositions of the velocity-resolved time-lag response in these objects may be accomplished using the maximum entropy method (Horne et al. 1991; Horne 1994).
5. We are able to confirm several trends in the behavior of the broad optical recombination lines that are expected from recent photoionization calculations and have also typically been seen in other AGN monitoring campaigns. Specifically, we confirm an increase in responsivity and a decrease in the mean time lag as the excitation and ionization level for an emission line increases. This is manifest as τ(Hα) > τ(Hβ) > τ(Hγ) > τ(He I) > τ(He II) and η(Hα) < η(Hβ) < η(Hγ) < η(He I)< η(He II). Agreement with these photoionization calculations argues for optical-depth effects that appear to "fine tune" the responses of the optical recombination lines, as expected under the LOC model for AGN BLRs.

Many of the additional predictions of Korista & Goad (2004) for optical recombination lines in AGN BLRs require multiple monitoring campaigns of multiple emission lines from a single AGN in different flux states. The investment of time to examine these predictions is both warranted and necessary. The optical recombination line emissivities and responsivities depend on the local continuum flux (i.e., radius) for a fixed continuum luminosity, and thus the optical recombination lines are important to include in quasar tomography for mapping out the physical parameters of BLR (Horne et al. 2003). The recovery of a velocity-delay map for a single emission line, such as Hβ, is a key goal of reverberation mapping and would allowing insight into the geometry and kinematics of the BLR. The simultaneous recovery of velocity-delay maps for several emission lines could set much stronger constraints on, and perhaps break degeneracies between, the physical parameters of the line-emitting gas in the BLR and may usher in yet another new era of understanding for this spatially unresolved region in AGNs.

We thank the excellent staff and support personnel at Lick Observatory for their enormous help during our observing run,

and Brad Peterson for helpful conversations and the use of his analysis software. We also thank Josh Shiode for his observing help. This work was supported by NSF grants AST–0548198 (UC Irvine), AST–0607485 and AST–0908886 (UC Berkeley), AST–0642621 (UC Santa Barbara), and AST–0507450 (UC Riverside). The UC Berkeley researchers also gratefully acknowledge the support of both the Sylvia & Jim Katzman Foundation and the TABASGO Foundation for the continued operation of KAIT. M.C.B. gratefully acknowledges support provided by NASA through Hubble Fellowhip grant HF–51251 and G.C. acknowledges support provided by NASA through grant GO-11101, both awarded by the Space Telescope Science Institute, which is operated by the Association of Universities for Research in Astronomy, Inc., for NASA, under contract NAS 5-26555.

REFERENCES

Antonucci, R. R. J., & Cohen, R. D. 1983, ApJ, 271, 564
Baldwin, J., Ferland, G., Korista, K., & Verner, D. 1995, ApJ, 455, L119
Bentz, M. C., et al. 2007, ApJ, 662, 205
Bentz, M. C., et al. 2008, ApJ, 689, L21 (Paper I)
Bentz, M. C., et al. 2009, ApJ, 705, 199 (Paper III)
Clavel, J., et al. 1991, ApJ, 366, 64
Cohen, R. D., Puetter, R. C., Rudy, R. J., Ake, T. B., & Foltz, C. B. 1986, ApJ, 311, 135
Dietrich, M., et al. 1993, ApJ, 408, 416
Ferland, G. J., Korista, K. T., Verner, D. A., Ferguson, J. W., Kingdon, J. B., & Verner, E. M. 1998, PASP, 110, 761
Ferland, G. J., & Mushotzky, R. F. 1982, ApJ, 262, 564
Gaskell, C. M., & Peterson, B. M. 1987, ApJS, 65, 1
Gaskell, C. M., & Sparke, L. S. 1986, ApJ, 305, 175
Horne, K. 1994, in ASP Conf. Ser. 69, Reverberation Mapping of the Broad-Line Region in Active Galactic Nuclei, ed. P. M. Gondhalekar, K. Horne, & B. M. Peterson (San Francisco, CA: ASP), 23
Horne, K., Korista, K. T., & Goad, M. R. 2003, MNRAS, 339, 367
Horne, K., Welsh, W. F., & Peterson, B. M. 1991, ApJ, 367, L5
Kaspi, S., Smith, P. S., Netzer, H., Maoz, D., Jannuzi, B. T., & Giveon, U. 2000, ApJ, 533, 631
Kollatschny, W. 2003, A&A, 407, 461
Korista, K. T., & Goad, M. R. 2000, ApJ, 536, 284
Korista, K. T., & Goad, M. R. 2004, ApJ, 606, 749 (erratum 627, 577 [2005])
Krolik, J. H., Horne, K., Kallman, T. R., Malkan, M. A., Edelson, R. A., & Kriss, G. A. 1991, ApJ, 371, 541
Kwan, J., & Krolik, J. H. 1981, ApJ, 250, 478
Landolt, A. U. 1992, AJ, 104, 340
McArthur, B., Jefferys, W., & McCartney, J. 1994, BAAS, 26, 900
Netzer, H. 1975, MNRAS, 171, 395
Onken, C. A., Ferrarese, L., Merritt, D., Peterson, B. M., Pogge, R. W., Vestergaard, M., & Wandel, A. 2004, ApJ, 615, 645
Onken, C. A., & Peterson, B. M. 2002, ApJ, 572, 746
Peterson, B. M., & Ferland, G. J. 1986, Nature, 324, 345
Peterson, B. M., Meyers, K. A., Carpriotti, E. R., Foltz, C. B., Wilkes, B. J., & Miller, H. R. 1985, ApJ, 292, 164
Peterson, B. M., & Wandel, A. 1999, ApJ, 521, L95
Peterson, B. M., Wanders, I., Horne, K., Collier, S., Alexander, T., Kaspi, S., & Maoz, D. 1998, PASP, 110, 660
Peterson, B. M., et al. 2004, ApJ, 613, 682
Peterson, B. M., et al. 2005, ApJ, 632, 799
Rees, M. J. 1984, ARA&A, 22, 471
Rees, M. J., Netzer, H., & Ferland, G. J. 1989, ApJ, 347, 640
Schlegel, D. J., Finkbeiner, D. P., & Davis, M. 1998, ApJ, 500, 525
van Groningen, E., & Wanders, I. 1992, PASP, 104, 700
Walsh, J. L., et al. 2009, ApJS, 185, 156 (Paper II)
White, R. J., & Peterson, B. M. 1994, PASP, 106, 879
Woo, J.-H., et al. 2010, ApJ, 716, 269